SOD1 is a synthetic lethal target in *PPM1D*-mutant leukemia cells

Linda Zhang[1,2,3,4,5], Joanne I. Hsu[1,2,3], Etienne D. Braekeleer[6], Chun-Wei Chen[3,4,5,7], Tajhal D. Patel[8], Alejandra G. Martell[4], Anna G. Guzman[4], Katharina Wohlan[4], Sarah M. Waldvogel[2,3,4,5,10], Hidetaka Urya[9], Ayala Tovy[3,4,5], Elsa Callen[11], Rebecca Murdaugh[3,4,5,12], Rosemary Richard[3,4,5,12], Sandra Jansen[13], Lisenka Vissers[13], Bert B.A. de Vries[13], Andre Nussenzweig[10], Shixia Huang[4,14], Cristian Coarfa[4], Jamie N. Anastas[3,4,5,12], Koichi Takahashi[9,14], George Vassiliou[6], Margaret A. Goodell*[,3,4,5]

1. Translational Biology and Molecular Medicine Graduate Program, Baylor College of Medicine, Houston, TX
2. Medical Scientist Training Program, Baylor College of Medicine, Houston, TX.
3. Stem Cells and Regenerative Medicine Center, Baylor College of Medicine, Houston TX
4. Department of Molecular and Cellular Biology, Baylor College of Medicine, Houston, TX
5. Center for Cell and Gene Therapy, Houston, TX
6. Department of Haematology, Wellcome-MRC Cambridge Stem Cell Institute, University of Cambridge
7. Integrated Molecular and Biomedical Sciences Graduate Program, Baylor College of Medicine, Houston, TX
8. Texas Children's Hospital Department of Hematology/Oncology, Baylor College of Medicine, Houston, TX
9. Department of Leukemia, The University of Texas MD Anderson Cancer Center, Houston, TX
10. Cancer and Cell Biology Graduate Program, Baylor College of Medicine, Houston, TX
11. Laboratory of Genome Integrity, National Cancer Institute, National Institute of Health, Bethesda, MD
12. Department of Neurosurgery, Baylor College of Medicine, Houston, TX
13. Donders Centre for Neuroscience, Radboud University Medical Center, Nijmegen, The Netherlands
14. Department of Education, Innovation and Technology, Advanced Technology Cores
15. Department of Genomic Medicine, The University of Texas MD Anderson Cancer Center, Houston, TX

***Corresponding Author:**
Margaret A. Goodell, Ph.D.
Professor and Chair
Department of Molecular and Cellular Biology
Director, Stem Cells and Regenerative Medicine Center
Vivian L. Smith Chair of Regenerative Medicine
Baylor College of Medicine
One Baylor Plaza, BCM N1030
Houston, TX 77030
713-798-6037
goodell@bcm.edu

Abstract

The DNA damage response is critical for maintaining genome integrity and is commonly disrupted in the development of cancer. PPM1D (protein phosphatase, Mg2+/Mn2+ dependent 1D) is a master negative regulator of the response; gain-of-function mutations and amplifications of *PPM1D* are found across several human cancers making it a relevant pharmacologic target. Here, we used CRISPR/Cas9 screening to identify synthetic-lethal dependencies of *PPM1D,* uncovering superoxide dismutase-1 (SOD1) as a potential target for PPM1D-mutant cells. We revealed a dysregulated redox landscape characterized by elevated levels of reactive oxygen species and a compromised response to oxidative stress in *PPM1D*-mutant cells. Altogether, our results demonstrate the protective role of SOD1 against oxidative stress in *PPM1D*-mutant leukemia cells and highlight a new potential therapeutic strategy against *PPM1D*-mutant cancers.

Introduction

Cellular DNA is frequently damaged by both endogenous and exogenous factors (Hoeijmakers, 2009). Unresolved DNA damage can lead to genomic instability, which is a hallmark of aging and cancer (Hanahan and Weinberg, 2011). Cells have evolved intricate mechanisms to detect and repair DNA lesions. The DNA damage response (DDR) is a complex network of signaling pathways that coordinate various cellular processes initiated by p53, such as DNA repair (Ciccia and Elledge, 2010), cell cycle checkpoint activation (Harper et al., 1993), and apoptosis (Yonish-Rouach et al., 1991). However, upon resolution of DNA damage, the cell must terminate the DDR to avoid prolonged cell cycle arrest and apoptosis. One critical mechanism for DDR termination is the expression of Protein Phosphatase Mg^{2+}/Mn^{2+}–Dependent 1D (PPM1D) (Fiscella et al., 1997), which is induced by p53 and plays a key role in attenuating the response. PPM1D is a member of the PP2C family of serine/threonine protein phosphatases and has been shown to dephosphorylate a wide range of DDR signaling molecules including p53, p38 MAPK, CHK1, CHK2, and H2AX (Bulavin et al., 2002; Cha et al., 2010; Lu et al., 2005; Oliva-Trastoy et al., 2007; Takekawa et al., 2000). These dephosphorylation events generally lead to reduced activity of the targets, ultimately resulting in deactivation of the DDR.

Dysregulation of PPM1D has been associated with the development of diverse cancers, including breast, ovarian, esophagus, brain, and others (Khadka et al., 2022; Li et al., 2002; Li et al., 2020b; Ruark et al., 2013; Zhang et al., 2014). *PPM1D* is located on chromosome 17q and therefore frequently amplified in breast and ovarian cancers exhibiting 17q23 amplifications (Li et al., 2002; Ruark et al., 2013). These amplifications result in overexpression of the wildtype PPM1D protein and consequently leads to suppression of p53 and other PPM1D targets in the DDR (Bulavin et al., 2002; Lambros et al., 2010). In addition, PPM1D can also become dysregulated through mutations in its terminal exon. These mutations produce a truncated protein that is stabilized, evading proteasome-mediated degradation (Tokheim et al., 2021). The resulting mutant protein maintains its phosphatase activity and is found at high levels even in the absence of DNA damage. Excessive PPM1D activity leads to constitutive dephosphorylation and downregulation of PPM1D targets including multiple members of the DDR (Hsu et al., 2018). These gain-of-function *PPM1D* mutations are observed in diverse solid cancers including osteosarcoma (He et al., 2021), colorectal carcinoma (Peng et al., 2014; Yin et al., 2013), diffuse midline gliomas (Wang et al., 2011; Zhang et al., 2014) and others. Moreover, *PPM1D* mutations and overexpression are associated with advanced tumor stage, worse prognosis, and increased lymph node metastasis (Fu et al., 2014; Jiao et al., 2014; Li et al., 2020a; Li et al., 2020b; Peng et al., 2014; Zhang et al., 2014).

More recently, *PPM1D*-mutations have been shown to drive expansion of hematopoietic stem cells (Bolton et al., 2020; Hsu et al., 2018; Kahn et al., 2018) in association with clonal hematopoiesis (CH), a pre-malignant state associated with an increased risk of hematologic malignancies and elevated all-cause mortality (Genovese et al., 2014; Jaiswal et al., 2014). *PPM1D*-mutations are particularly enriched in patients with prior exposure to cytotoxic therapies, who have a high risk of therapy-related myeloid neoplasms (t-MN) (Hsu et al., 2018; Lindsley et al., 2017). Given the prevalence of *PPM1D* aberrations in cancer, PPM1D is an attractive therapeutic target. Ongoing efforts are focused on elucidating the structure of PPM1D to improve drug design and development (Miller et al., 2022). While several inhibitors thus far have shown efficacy *in vitro*, few have been studied *in vivo* and none have progressed to clinical trials due to poor bioavailability. Therefore, identifying targetable, synthetic-lethal partners to exploit the genetic defects of *PPM1D*-altered cells can offer an alternative therapeutic approach.

In this study, we performed an unbiased, whole-genome CRISPR screen to investigate genes essential for cell survival in *PPM1D*-mutated leukemia cell lines. We identified superoxide dismutase-1 (*SOD1*) as a novel synthetic-lethal dependency of PPM1D which was validated by genetic and pharmacologic approaches. We showed that the mutant cells display compromised responses to oxidative stress and DNA damage, leading to increased reactive oxygen species and genomic instability. These results provide valuable insights into the biological processes corrupted by mutant PPM1D and underscore the potential of SOD1 as a targetable vulnerability in this context.

Results

SOD1 is a synthetic lethal vulnerability of *PPM1D*-mutant leukemia cells

CRISPR dropout screens have emerged as a powerful tool to assess the functional importance of individual genes within a particular pathway by measuring the impact of their depletion on cell viability or fitness. To identify genes essential for *PPM1D*-mutant cell survival, we first created isogenic wild-type (WT) and *PPM1D*-mutant Cas9-expressing OCI-AML2 leukemia cell lines and selected two *PPM1D*-mutant clones for CRISPR screening (**Figure 1–figure supplement 1A**). We transduced the cells with a whole-genome lentiviral library containing 90,709 guide RNAs (gRNAs) targeting 18,010 human genes (Tzelepis et al., 2016). At day ten post-transduction, the cells were harvested for the first timepoint and then subsequently passaged for an additional 18 days to allow for negatively selected gene-knockout cells to “drop out”. The remaining pool of cells were collected for deep sequencing analysis of gRNA abundance (**Figure**

125 **1A**). We analyzed genes that were specifically depleted in the mutant but not WT cells using the
126 MaGECK-VISPR pipeline (Li et al., 2014). Differentially depleted genes are those for which the
127 knockout or depletion of the gene results in a significant impact on the viability or growth of
128 *PPM1D*-mutant cells compared to WT control cells. Through this analysis, we identified 409
129 differentially depleted genes in one of the *PPM1D*-mutant clones and 92 differentially depleted
130 genes in the other clone while adhering to the maximum false discovery rate (FDR) cutoff of 25%.
131 Among these genes, we found 37 common candidates that were depleted in both *PPM1D*-mutant
132 biological replicates that were not depleted in the WT control cells **(Figure 1–figure supplement**
133 **1B, Figure 1–source data 1)**.
134 Gene ontology analysis of these top essential genes demonstrated an enrichment in
135 pathways related to DNA repair, interstrand crosslink (ICL) repair, and cellular responses to stress
136 (**Figure 1B**). Pathway analyses with the KEGG and REAC databases revealed a significant
137 enrichment of the Fanconi anemia (FA) repair pathway, with notable genes such as *BRIP1*
138 (*FANCJ*), *FANCI, FANCA, SLX4* (*FANCP), UBE2T* (*FANCT*), and *C19orf40 (FAAP24)* **(Figure**
139 **1–figure supplement 1C)**. Interestingly, our dropout screen revealed that superoxide dismutase
140 [Cu/Zn], or *SOD1*, was the top essential gene based on fitness score (**Figure 1C**). SOD1 is a
141 crucial enzyme involved in scavenging superoxide (O_2^-) radicals, which are harmful byproducts
142 of mitochondrial cellular metabolism. Excessive reactive oxygen species (ROS) causes oxidative
143 stress, which can damage cellular structures including DNA, proteins, and lipids. SOD1 is an
144 attractive therapeutic target due to the availability of SOD1 small molecule inhibitors that are being
145 tested in clinical trials (Lin et al., 2013; Lowndes et al., 2008). Therefore, we decided to further
146 investigate the role of SOD1 in promoting *PPM1D*-mutant cell survival.
147 To validate the essentiality of SOD1 in *PPM1D*-mutant cells, we performed *in vitro*
148 competitive proliferation assays in two different acute myeloid leukemia (AML) cell lines, OCI-
149 AML2 and OCI-AML3. We transduced isogenic WT and *PPM1D*-mutant Cas9-expressing cells
150 with either empty vector (EV) or sg*SOD1*-expressing lentiviral vectors containing a blue-
151 fluorescent protein (BFP) reporter. We validated the loss of SOD1 protein expression by western
152 blot (**Figure 1 – figure supplement 1D**) and confirmed that transduction of the empty vector
153 control did not alter cellular fitness (**Figure 1 – figure supplement 1E**). While loss of *SOD1* had
154 minimal effects on the fitness of WT cells, *PPM1D*-mutant cells with *SOD1* deletion had significant
155 reduction in cellular growth in both OCI-AML2 and OCI-AML3 cells *in vitro* (**Figure 1D**).
156 To test if *SOD1*-deletion affected the fitness of $PPM1D^{mut}$ vs WT leukemia cells *in vivo*,
157 we transplanted *PPM1D*-mutant and -WT OCI-AML2 cells with or without *SOD1* deletion into
158 immunodeficient (NSG) mice. Mice transplanted with control *PPM1D*-mutant and -WT cells (with

159 intact SOD1) had a similar median survival of 32 days. When *SOD1* was deleted, the survival of
160 mice transplanted with PPM1D-WT leukemia cells increased to a median of 43 days. Importantly,
161 the survival of mice transplanted with *PPM1D*^{mut}-*SOD1*$^{-/-}$ cells was even more significantly
162 extended to a median time of 55 days (**Figure 1E**). These data provide an *in vivo* validation of the
163 CRISPR screen demonstrating a differential dependency between *PPM1D*-mutant vs -WT cells
164 on SOD1. Broadly, these results show that loss of *SOD1* confers a disadvantage to leukemia cells
165 that is markedly amplified in the context of the PPM1D truncating mutation.
166

167 ***PPM1D*-mutant cells are sensitive to SOD1 inhibition and have increased oxidative 168 stress**

169 We next wanted to test if pharmacologic inhibition of SOD1 could mimic the genetic
170 deletion of *SOD1*. We used two different SOD1 inhibitors, 4,5-dichloro-2-m-tolyl pyridazin-3(2H)-
171 one (also known as lung cancer screen-1, or LCS-1) and *Bis*-choline tetrathiomolybdate (ATN-
172 224), which work by different mechanisms. LCS-1 is a small molecule that binds to SOD1 and
173 disrupts its activity (Somwar et al., 2011), while ATN-224 is a copper chelator that reduces SOD1
174 activity by decreasing the availability of copper ions, which are an essential SOD1 cofactor
175 (Juarez et al., 2006).
176 To study the sensitivity of the mutant cells to SOD1 inhibition, we engineered truncating
177 *PPM1D* mutations into three patient-derived AML cell lines, MOLM-13, OCI-AML2, and OCI-
178 AML3, which harbor distinct genetic backgrounds and AML driver mutations. At baseline, we
179 found that *PPM1D*-mutant cells had increased SOD activity compared to WT cells and confirmed
180 that SOD activity was significantly inhibited upon treatment with ATN-224 in a dose-dependent
181 manner (**Figure 2–figure supplement 1A**). In addition, ATN-224 induced a significantly greater
182 proportion of apoptotic *PPM1D*-mutant than *PPM1D*-WT cells (**Figure 2–figure supplement 1B**).
183 *PPM1D*-truncating mutations conferred significant sensitivity to SOD1 inhibition compared to their
184 WT counterparts in all three AML cell lines **(Figure 2A, Figure 2–figure supplement 2A**). To
185 determine if this cytotoxicity was dependent on oxidative stress, we treated the cells with SOD1
186 inhibitors in combination with an antioxidant, N-acetylcysteine (NAC). Importantly, NAC
187 supplementation was able to completely rescue the sensitivity of mutant cells to both LCS-1 and
188 ATN-224 treatment (**Figure 2B, Figure 2–figure supplement 1C**), suggesting that ROS
189 generation contributes to the sensitivity of mutant cells to SOD1 inhibition.
190 Activating mutations in oncogenes often lead to increased ROS generation by altering
191 cellular metabolism, inducing replication stress, or dysregulating redox homeostasis (Maya-

192 Mendoza et al., 2015; Park et al., 2014). We therefore hypothesized that *PPM1D*-mutant cells
193 have increased oxidative stress, leading to reliance on SOD1 for protection. SOD1 catalyzes the
194 breakdown of superoxide into hydrogen peroxide and water. Therefore, we assessed cytoplasmic
195 and mitochondrial superoxide levels using dihydroethidium and Mitosox Green, respectively.
196 These fluorogenic dyes are rapidly oxidized by superoxide, but not other types of ROS, to produce
197 green fluorescence. We observed that in the absence of exogenous stressors, *PPM1D*-mutant
198 cells had a moderate increase in superoxide radicals (**Figure 2C, Figure 2–figure supplement**
199 **1C**). SOD2 is the primary superoxide dismutase in the mitochondria responsible for catalyzing
200 superoxide into H_2O_2. Given the increase in mitochondrial superoxide levels, we assessed levels
201 of SOD2 protein levels. Surprisingly, there were no baseline differences or compensatory
202 changes in SOD2 after *SOD1* deletion (Figure 2–figure supplement 2C).

203 Free radicals can be detrimental to cells due to their ability to oxidize proteins, lipids, and
204 DNA. Therefore, we also measured levels of lipid peroxidation as an additional measure of
205 oxidative stress. Consistent with the increase in superoxide radicals, we observed a concurrent
206 increase in lipid peroxidation in the *PPM1D*-mutant cells **(Figure 2D**). Using 2'7'-
207 dichlorofluorescein diacetate (DCFDA) staining to measure total ROS levels, we observed that
208 *PPM1D*-mutant cells harbored more total ROS compared to WT cells (**Figure 2E**).

209 To investigate whether the observed elevated ROS was a characteristic of other *PPM1D*-
210 mutant cell lines, we measured ROS levels in two different germline models. Humans with
211 germline mutations in *PPM1D* were first described by Jansen et al. in 2017 in patients with
212 intellectual disability. This neurodevelopmental condition is named Jansen-de Vries syndrome
213 (JdVS, OMIM #617450) and is characterized by frameshift or nonsense mutations in the last or
214 second-to-last exons of the *PPM1D* gene. These mutations result in functionally active, truncated
215 mutant proteins like those exhibited in human cancers and clonal hematopoiesis. Lymphoblastoid
216 cell lines (LCLs) were generated from these JdVS patients by Jansen et al (Jansen et al., 2017;
217 Wojcik et al., 2023).

218 In addition to human *PPM1D*-mutant LCLs, we also generated mouse embryonic
219 fibroblasts (MEFs) from a germline mouse model harboring a heterozygous truncating mutation
220 in the terminal exon of *Ppm1d (Hsu et al., 2018)*. When we measured total ROS from both the
221 JdVS LCLs and the *Ppm1d*-mutant MEFs compared to their WT counterparts, both mutant models
222 exhibited greater levels of total ROS (**Figure 2–figure supplement 2D, 2E**). Additionally,
223 *PPM1D*-mutant LCLs were also more sensitive to pharmacologic SOD1 inhibition compared to
224 the WT LCL line, GM12878 (**Figure 2–figure supplement 2F**). These results demonstrate that

225 *PPM1D* mutations not only increase ROS in the context of cancer, where cellular metabolism is
226 often altered, but can also alter redox homeostasis in non-transformed cells.
227 To determine if mutant PPM1D was associated with ROS generation, we treated isogenic
228 OCI-AML2 WT and *PPM1D*-mutant cells with a PPM1D inhibitor, GSK2830371, for 24 hours. We
229 found that pharmacologic inhibition of PPM1D mildly decreased ROS levels in both WT and
230 *PPM1D* mutant cells (**Figure 2F**), suggesting a link between PPM1D and ROS production.
231 Altogether, these data demonstrate that SOD1 inhibition leads to cytotoxicity in the mutant cells
232 due to increased oxidative stress induced by mutant PPM1D.
233

234 ## ***PPM1D*-mutant leukemia cells have altered mitochondrial function**

235 Mitochondria are the primary source of ROS within the cell, as the electron transport chain
236 is a major site of ROS production during oxidative phosphorylation. We next asked whether the
237 observed increase in ROS in *PPM1D*-mutant cells was due to differences in mitochondrial
238 abundance. We used two independent methods to measure mitochondrial mass, including
239 MitoTracker Green flow cytometry (**Figure 3A**) and western blot analysis of mitochondrial
240 complex proteins (**Figure 3B**). However, we did not observe a difference in mitochondrial mass
241 with either method. This finding suggests that mechanisms other than a change in mitochondrial
242 abundance are responsible for the increase in ROS levels in mutant cells, such as alterations in
243 mitochondrial metabolism or changes in ROS scavenging systems.
244 To assess mitochondrial function, we performed seahorse assays in WT and *PPM1D*-
245 mutant cells. Our seahorse assays revealed that the mutant cells have decreased mitochondrial
246 respiration, as indicated by decreased basal, maximal, and ATP-linked respiration (**Figure 3C**).
247 While *PPM1D*-mutant MOLM-13 and OCI-AML3 cells also had decreased basal respiration, there
248 were variable differences in maximal and ATP-linked respiration compared to WT, suggesting
249 possible cell line differences affecting mitochondrial respiration **(Figure 3–figure supplement 1A,**
250 **B**)**.** In addition to analyzing respiratory capacity, we also examined mitochondrial membrane
251 potential (MMP) using the fluorescent dye Mitotracker CMXRos, which accumulates in the
252 mitochondria in an MMP-dependent manner. We stained both WT and mutant cells with
253 Mitotracker CMXRos and observed a decrease in MMP in the mutant cells (**Figure 3D**). Tracking
254 cell numbers between the WT and mutant cell lines over time established this decrease in MMP
255 was not due to altered cellular growth rates (**Figure 3–figure supplement 1C**). Altogether, these
256 findings, along with decreased respiratory capacity and increased mitochondrial ROS, indicate a
257 mitochondrial defect in *PPM1D*-mutant cells.

PPM1D-mutant cells have a reduced oxidative stress response

Mitochondrial dysfunction and increased ROS production are closely intertwined. On one hand, mitochondrial dysfunction leads to increased ROS production as a result of impaired oxidative phosphorylation and increased electron leakage (Turrens, 2003). On the other hand, sustained oxidative stress can directly damage mitochondrial components and mtDNA and compromise their function (Wallace, 2005). To better understand the molecular basis for the observed mitochondrial dysfunction and dependency on SOD1, we performed bulk RNA-sequencing (RNA-seq) on Cas9-expressing WT and *PPM1D*-mutant OCI-AML2 cells transduced with *SOD1*-sgRNA to induce *SOD1* deletion or the empty vector (EV) control (**Figure 4–figure supplement 1A**). Both EV and SOD1-sgRNA vectors were tagged with a BFP reporter to identify transduced cells. The cells were collected ten-days post-transduction, the timepoint at which we observed 50% reduction of the *SOD1*-deletion cells during the *in vitro* proliferation assays, reasoning this would capture the effects of *SOD1*-deletion on cellular and metabolic processes while avoiding excessive cell death.

Analysis of the RNA-seq data revealed 2239 differentially expressed genes, with 1338 downregulated genes and 901 upregulated genes in the mutant cells compared to WT cells at baseline (**Figure 4–source data 1**). Gene set enrichment analysis (GSEA) of the differentially expressed genes showed an upregulation in genes related to cell cycle (GO: 0007049), cell division (GO: 0051301), DNA replication (GO: 005513), and mitophagy (GO: 0000423) in the *PPM1D*-mutant cells (**Figure 4A**). Interestingly, there was a significant downregulation of pathways related to the regulation of the oxidative stress response (GO: 1902882, **Figure 4–figure supplement 1B**), ROS metabolic processes (GO: 0072593), and oxidation reduction (GO: 0055114). Following *SOD1* deletion, the WT cells displayed notable upregulation of pathways associated with cell cycling, chromosome organization, cell division, and DNA repair. In contrast, the mutant cells showed significant downregulation of these same pathways (**Figure 4–figure supplement 1C**). Intriguingly, upon *SOD1* deletion, the mutant cells exhibited an upregulation in the response to oxidative stress (GO:0006979, **Figure 4–figure supplement 1D**). This finding suggests a reactive transcriptional response to the heightened ROS levels resulting from the loss of SOD1.

As PPM1D is a phosphatase that can directly modulate the activation state of proteins, we examined whether there were alterations in protein and phosphoprotein levels in *PPM1D*-mutant cells using reverse phase protein array (RPPA) analysis, mirroring the experimental design used for bulk RNA-seq (**Figure 4–figure supplement 1A**). By focusing on differential protein expression between wild-type (WT) and *PPM1D*-mutant cells, we aimed to capture the post-

translational regulatory events that could contribute to the mitochondrial dysfunction observed in the mutants. The RPPA analysis of over 200 (phospho-)proteins covering major signaling pathways identified 128 differentially expressed proteins between *PPM1D*-mutant and control WT OCI-AML2 cells (a panel of 264 proteins), with 67 downregulated proteins and 61 upregulated proteins (**Figure 4–figure supplement 2A, source data 2**). Notably, over-representation analysis showed that among the differentially expressed proteins, there was a significant enrichment in the "Response to Oxidative Stress" pathway in the mutant cells (-log10(pValue) = 24.164) compared to WT, with a particular emphasis on the downregulated proteins of this pathway (-log10(pValue 15.457, **Figure 4B**, **Figure 4–source data 3**). While the RNA-seq suggested a transcriptional upregulation of the response to oxidative stress in the mutant cells after *SOD1* deletion, the RPPA data revealed that the mutant cells continued to exhibit decreased expression in proteins associated with the oxidative stress response (**Figure 4–figure supplement 2B**). Taken together, these findings suggest that *PPM1D*-mutant cells have an inherent impairment in their baseline response to oxidative stress.

To further explore the diminished oxidative stress response in the mutant cells, we assessed their total- and small-molecule-antioxidant capacity. Total antioxidant capacity refers to the overall ability of the cells to counteract free radicals and reduce oxidative damage. This includes enzymatic antioxidants such as catalase, SODs, and peroxidases. Small molecule antioxidant capacity measures the capacity of low molecular weight antioxidants, such as glutathione and vitamin E, to neutralize ROS (Hawash et al., 2022). Our results showed that *PPM1D*-mutant cells have significantly reduced total and small-molecule antioxidant capacity compared to WT cells (**Figure 4C**).

Subsequently, we measured intracellular glutathione (GSH), a pivotal antioxidant crucial for maintaining cellular redox balance and protecting against oxidative stress. Strikingly, our analysis revealed a higher proportion of mutant cells with diminished GSH levels compared to their WT counterparts (**Figure 4D**). We also measured the protein levels of key antioxidant enzymes by western blot. While we saw similar protein levels of SOD1 in both WT and mutant cells, we observed a reduction in the thioredoxin and catalase levels (**Figure 4E**). These results provide evidence to support the RNA-seq and RPPA findings that *PPM1D*-mutant cells have impaired antioxidant defense mechanisms, leading to an elevation in ROS levels and reliance on SOD1 for protection.

PPM1D mutations increase genomic instability and impair non-homologous end-joining repair

In addition to a decreased response to oxidative stress, the RNA-seq GSEA analysis also revealed differential responses to DNA repair. Upon *SOD1* deletion, WT cells significantly upregulated the regulation of DNA repair (GO:0006281), double-stranded break repair (GO:0006302), homologous recombination (GO:0035825), and more. However, there was a striking downregulation of DNA repair pathways after deletion of *SOD1* in the mutant cells (**Figure 4–figure supplement 1C**). PPM1D plays a key role in suppressing the DNA damage response (DDR) by dephosphorylating, thereby inactivating, p53 and other key upstream and downstream effectors of the pathway. Truncating mutations and amplifications in *PPM1D* that lead to increased PPM1D activity may therefore inhibit DNA damage repair and increase genomic instability. Oxidative stress and ROS also pose endogenous challenges to genomic integrity. Therefore, we hypothesized that due to the increase in ROS within the mutant cells, loss of *SOD1* may lead to unsustainable accumulation of DNA damage and overwhelm the mutant cell's DNA repair capacity.

To test this hypothesis, we first sought to establish the baseline levels of DNA damage in *PPM1D*-altered cells. We performed alkaline comet assays in mouse embryonic fibroblasts and found a significant increase in single- and double-stranded DNA breaks in mutant cells compared to WT (**Figure 5A**). As ROS are known to contribute to oxidative DNA damage, we further assessed the levels of 8-oxo-2′-deoxyguanosine (8-oxo-dG), a well-established marker of oxidative DNA damage. Strikingly, the mutant cells demonstrated elevated levels of oxidative DNA damage at baseline (**Figure 5B**). We also performed metaphase spreads in mouse primary B-cells to investigate chromosomal aberrations, which are consequences of abnormal double-stranded break repair. WT and *Ppm1d*-mutant mouse primary resting CD43+ B-cells were purified from spleens and stimulated with LPS, IL-4, and CD180 to induce proliferation. The cells were then treated with either low- or high-dose cisplatin for 16-hours. Consistent with our comet assay findings, we observed that *Ppm1d*-mutant cells harbored approximately two-fold more chromosomal breaks per metaphase after exposure to cisplatin (**Figure 5C**). When we classified the chromosomal aberrations into subtypes, we observed that the mutant cells had increased numbers of each type of aberration. These results demonstrate that mutations in *PPM1D* increase genomic instability.

To further assess the DNA repair efficiency of *PPM1D*-mutant cells, we utilized U2OS DNA repair reporter cell lines which express a green fluorescent protein (GFP) cassette when

specific DNA repair pathways are active after stimulation when the I-SceI restriction enzyme is induced to stimulate a double-stranded break (DSB). To test for homologous recombination (HR), tandem defective GFP genes can undergo HR to generate GFP+ cells. Non-homologous end joining (NHEJ) repairs a defective GFP in a distinct cassette (Weinstock et al., 2006). Because the U2OS parental line harbors an endogenous heterozygous *PPM1D* truncating mutation (R458X) (Kleiblova et al., 2013), we corrected the lines to generate the isogenic *PPM1D* WT control (**Figure 5–figure supplement 1A**).

With two isogenic clones for each reporter cell line, we transfected the *PPM1D*-WT and -mutant U2OS clones with I-SceI and measured GFP expression by flow cytometry after 48 hours. Our results showed similar levels of HR-mediated repair in both WT and mutant clones (**Figure 5D**). Prior studies have shown that WT PPM1D promotes HR by forming a stable complex with BRCA1-BARD1, thereby enhancing their recruitment to DSB sites (Burdova et al., 2019). Although gain-of-function mutations in PPM1D lead to persistent PPM1D activity, it may not necessarily result in increased HR repair. Several factors can limit the extent of HR enhancement. For instance, HR is typically restricted to the S/G2 phase of the cell cycle and is a multi-step process that beings with DNA end resection (Xu and Xu, 2020). This is a crucial initial step that generates single-stranded DNA overhangs to facilitate strand invasion and recombination (Gnugge and Symington, 2021). Therefore, the impact of mutant PPM1D on HR may be constrained by the efficiency of DNA end resection and cell cycling, among other regulatory mechanisms within the HR pathway.

In contrast, we saw significantly decreased NHEJ repair in the *PPM1D*-mutant clones (**Figure 5E**). This downregulation of NHEJ may be due to diminished activation of yH2AX and ATM. These two proteins serve as key upstream regulators within the DDR and are subject to dephosphorylation by PPM1D (Cha et al., 2010; Lu et al., 2005). In addition, prior studies have also shown that PPM1D modulates lysine-specific demethylase 1 (LSD1) activity, which is important for facilitating the recruitment of 53BP1 to DNA damage sites through RNF168-dependent ubiquitination (Peng et al., 2015). *PPM1D* mutations may therefore lead to impairment of NHEJ through dysregulation of 53BP1 recruitment. To confirm this, we performed immunofluorescence imaging of Rad51 and 53BP1 foci. The recruitment of Rad51 and 53BP1 to the sites of DNA damage are important for the activation of HR and NHEJ, respectively. We analyzed mouse embryonic fibroblasts at baseline and after irradiation (10 Gy) and observed similar numbers of Rad51 foci in *Ppm1d*-mutant and WT cells (**Figure 5–figure supplement 1B**). In contrast, *Ppm1d*-mutant MEFs had fewer 53BP1 foci, indicating decreased NHEJ repair capacity that was consistent with our U2OS reporter line findings (**Figure 5–figure supplement**

391 **1C**). Comet assays were performed in parallel with the immunofluorescence experiments to show
392 that the mutant cells had increased DNA damage (**Figure 5–figure supplement 1D**). Therefore,
393 the decrease in foci was not due to resolution of DNA damage, but rather due to inefficient DNA
394 repair.

395 In light of the elevated levels of DNA damage and compromised DNA repair observed in
396 the *PPM1D*-mutant cells, we hypothesized that loss of SOD1 may exacerbate genomic instability,
397 ultimately leading to mutant cell death. To assess this hypothesis, we performed comet assays
398 after *SOD1* deletion. Contrary to our hypothesis, genetic deletion of *SOD1* did not result in a
399 significant increase in DNA breaks in neither WT nor mutant cells (**Figure 5F**). These results
400 suggest that the vulnerability of *PPM1D*-mutant cells to SOD1 loss is not necessarily mediated
401 by an exacerbation of DNA damage but rather by other consequences of oxidative stress and
402 ROS imbalance.

403 Discussion

404 The search for synthetic-lethal strategies for cancer therapy has gained significant
405 attention in recent years due to the potential to identify new therapeutic targets that exploit tumor-
406 specific vulnerabilities. In this study, we performed whole-genome CRISPR/Cas9 screening to
407 uncover synthetic-lethal partners of *PPM1D*-mutant leukemia cells. Our screen revealed that
408 *SOD1* was the top essential gene for *PPM1D*-mutant cell survival, a dependency that was
409 validated *in vivo*. Ongoing efforts are underway to develop SOD1 inhibitors for the treatment of
410 cancer and ALS (Abati et al., 2020; Huang et al., 2000), and it is conceivable these may be useful
411 in the context of *PPM1D* mutation.

412 To explore this concept, we tested the sensitivity of WT and *PPM1D*-mutant cells to known
413 SOD1 inhibitors ATN-224 and LCS-1. We found that *PPM1D*-mutant cell lines were significantly
414 more sensitive to these compounds compared to WT. This sensitivity could be rescued upon
415 supplementation with the antioxidant, NAC, consistent with a role in reducing the impact of
416 reactive oxygen species. However, given potential off-target effects of LCS-1 (Ling et al., 2022;
417 Steverding and Barcelos, 2020) we cannot verify that the cytotoxic effects are via its activity
418 toward SOD1. Similarly, we cannot rule out that effects of ATN-224 are not due to other effects
419 caused by copper chelation (Chidambaram et al., 1984; Lee et al., 2013; Lowndes et al., 2008;
420 Lowndes et al., 2009). Further work to determine the potential of SOD mimetics like TEMPOL and
421 MnTBAP in mitigating the effects of SOD1 inhibition would be valuable in confirming the specificity
422 of the inhibitors for our underlying phenotype.

423 We also investigated the mechanisms underlying the dependency on SOD1 and
424 characterized the redox landscape of *PPM1D*-mutant cells, which revealed significant oxidative
425 stress and mitochondrial dysfunction. Recent studies have suggested that PPM1D is indirectly
426 associated with energy metabolism via dephosphorylation of the ataxia telangiectasia mutated
427 (ATM) protein. ATM promotes mitochondrial homeostasis, and therefore sustained inactivation of
428 ATM could lead to potential mitochondrial dysfunction (Bar et al., 2023; Guleria and Chandna,
429 2016; Valentin-Vega et al., 2012). However, oxidative stress and mitochondrial dysfunction are
430 closely related, and it is difficult to dissect the driving factor. We therefore performed RNA-
431 sequencing and RPPA analysis to better understand the underlying processes contributing to the
432 heightened oxidative stress observed in the mutant cells. Our analyses indicated a diminished
433 response to oxidative stress in the mutant cells. These findings may suggest a self-amplifying
434 cycle whereby dysregulation of ROS scavenging systems increases ROS levels, which in turn
435 leads to mitochondrial dysfunction, which further exacerbates oxidative stress. Hence, the
436 additional impairment of ROS detoxification mechanisms within the cell, such as the loss of SOD1,
437 has detrimental consequences for the viability of mutant cells.
438 The loss of SOD1 leads to increased O_2^- levels and reduced intracellular H_2O_2. These two
439 ROS species play especially important roles as signaling messengers that control cellular
440 proliferation, differentiation, stress responses, inflammatory responses, and more (Sauer et al.,
441 2001; Sies and Jones, 2020; Thannickal and Fanburg, 2000). These effects are mediated through
442 the reversible oxidation and reduction of cysteine residues (Poole, 2015) that have significant
443 effects on key signaling proteins including Erk1/2, protein phosphatases, and more. Therefore,
444 while ROS levels may be significantly impacted by the loss of SOD1, we cannot rule out the
445 possibility of altered ROS-driven signaling, rather than ROS-induced damage, as an underlying
446 mechanism for our results.
447 Multiple mechanisms may underlie the suppressed oxidative stress response observed in
448 *PPM1D*-mutant cells. One possible explanation is through PPM1D-mediated inhibition of p53.
449 p53 exhibits complex and context-dependent roles in cellular responses to oxidative stress, and
450 its functions can vary depending on the severity of stress encountered by the cell (Kang et al.,
451 2013; Liang et al., 2013; Sablina et al., 2005). Under mild or moderate oxidative stress conditions,
452 p53 may protect the cell from ROS by inducing the transcription of genes such as superoxide
453 dismutase (SOD), glutathione peroxidase (GPx), and others (Dhar et al., 2011; Peuget et al.,
454 2014; Sablina et al., 2005; Tan et al., 1999). However, under severe or prolonged oxidative stress,
455 the pro-apoptotic functions of p53 may promote ROS production to eliminate cells that have
456 accumulated excessive DNA damage or irreparable cellular alterations. The duality of these anti-

457 and pro-oxidant functions of p53 highlight its intricate role in modulating responses to oxidative
458 stress. How PPM1D affects the switch between these functions of p53 is not understood.
459 Furthermore, the extent to which the dependency on SOD1 observed in *PPM1D*-mutant cells is
460 mediated through p53 remains unclear and requires deeper exploration to better understand the
461 context in which SOD1 inhibitors can be used in cancer therapy.

462 Oxidative stress and DNA damage are intimately linked processes that frequently co-occur.
463 Our study also investigated the interplay between PPM1D, DNA damage, and oxidative stress.
464 We demonstrated significant genomic instability of *PPM1D*-mutant cells at baseline and further
465 characterized the effects of mutant PPM1D on specific DNA repair pathways. While previous
466 studies have suggested a role for PPM1D in modulating HR and NHEJ (Burdova et al., 2019;
467 Peng et al., 2015), our study is the first to demonstrate impaired NHEJ in *PPM1D*-mutant cells.
468 Additionally, our study corroborated previous research demonstrating the synthetic-lethal
469 relationship of *SOD1* and other DNA damage genes such as *RAD54B, BLM,* and *CHEK2 (Sajesh*
470 *et al., 2013; Sajesh and McManus, 2015)*. However, *SOD1*-deletion did not exacerbate DNA
471 damage, suggesting that the vulnerability of *PPM1D*-mutant cells to SOD1 loss cannot be
472 explained by increased DNA damage and may be more likely due to consequences of oxidative
473 stress. Recent studies have shown that ATN-224 can enhance the anti-tumor effects of cisplatin
474 by increasing ROS, decreasing glutathione content, and increasing DNA damage (Li et al., 2022).
475 These results highlight the potential for combinatorial therapies to achieve therapeutic synergism
476 and underscores the intricate relationship between ROS and DNA damage.

477 Interestingly, our screen also uncovered sensitivity of *PPM1D*-mutant cells to dropout of
478 genes in the Fanconi Anemia (FA) DNA repair pathway including *BRIP1* (*FANCJ*), *FANCI,*
479 *FANCA, SLX4* (*FANCP), UBE2T* (*FANCT*)*,* and *C19orf40 (FAAP24).* The FA pathway plays a
480 crucial role in facilitating the repair of interstrand crosslinks (Ceccaldi et al., 2016; Kottemann and
481 Smogorzewska, 2013). Outside of DNA repair and replication, there is a growing body of evidence
482 demonstrating mitochondrial dysfunction and redox imbalance in FA-patient cells (Korkina et al.,
483 1992). Several FA proteins are implicated in the maintenance of mitochondrial metabolism and
484 mitophagy (Cappelli et al., 2017; Kumari et al., 2014; Pagano et al., 2013; Sumpter et al., 2016).
485 Interestingly, a few studies have described a convergence in the FA pathway with SOD1. Early
486 work by Nordenson in 1977 found protective roles for SOD and catalase against spontaneous
487 chromosome breaks in cells from FA patients. Another study demonstrated mitochondrial
488 dysfunction, high ROS levels, and impaired ROS detoxification mechanisms in FA-deficient cell
489 lines(Kumari et al., 2014). Interestingly, *SOD1* expression increased in response to H_2O_2
490 treatment in FA-intact cells, but not FA-deficient cells. These findings underscore the critical role

of the FA pathway in redox homeostasis by maintaining mitochondrial respiratory function and suppressing intracellular ROS production. Even more importantly, it demonstrates a convergence in the FA pathway with *SOD1*, providing further support for our CRISPR dropout screen results.

In summary, our investigation sheds light on the role of mutant PPM1D in modulating cellular responses to oxidative stress and DNA repair in leukemia cells, offering valuable insights into the underlying molecular mechanisms. This research not only enhances our understanding of PPM1D-mediated cellular responses, but also identifies potential therapeutic targets against *PPM1D*-mutant leukemia cells. However, it is important to acknowledge the limitations of our study. We recognize that while *PPM1D* mutations are frequently observed in patients with t-MN, they are rare in *de novo* AML (Hsu et al., 2018). While there is ample evidence that *PPM1D* is an oncogenic driver in many types of cancers (Ali et al., 2012; Khadka et al., 2022; Li et al., 2002; Nguyen et al., 2010; Wu et al., 2016), the clinical importance of targeting pre-malignant PPM1D-associated clonal expansion in the hematopoietic system is not clear. However, the prevalence of *PPM1D* somatic mutations in other tissues such as the esophagus, suggests the need for further investigation (Yokoyama et al., 2019).

506 # Materials and Methods
507
508 **Cell lines and Reagents**
509 Cas9-expressing OCI-AML2 cells were generated by lentiviral transduction using pKLV2-
510 EF1aBsd2ACas9-W plasmid obtained from Dr. Kosuke Yusa from the Sanger Institute (Addgene
511 #67978). Four days post-transduction, cells underwent blasticidin selection. Single clones were
512 obtained by fluorescence-activated cell sorting and functionally tested for Cas9 activity using a
513 lentiviral reporter pKLV2-U6gRNA5(gGFP)-PGKBFP2AGFP-W (Addgene #67980). *PPM1D*-
514 mutant cell lines were generated using the RNP-based CRISPR/Cas9 delivery method using a
515 single sgRNA (GCTAAAGCCCTGACTTTA). Single cells were sorted into 96-well, round-bottom
516 plates and expanded. Clones were validated by Sanger sequencing, TIDE analysis, and western
517 blot to visualize the overexpressed, truncated mutant protein. Two validated *PPM1D*-mutant
518 clones were selected for the CRISPR dropout screen.
519
520 **CRISPR Dropout Screen and Analyses**
521 For large-scale production of lentivirus, 15 cm plates of 80-90% confluent 293T cells were
522 transfected using Lipofectamine 2000 (Invitrogen) with 7.5 ug of the Human Improved Whole-
523 Genome Knockout CRISPR library V1 (by Kosuke Yuya, Addgene #67989), 18.5 ug of psPax2,
524 and 4 ug of pMD2.G. A lentivirus titer curve was performed prior to the screen to determine the
525 volume of viral supernatant to add for a multiplicity of infection (MOI) of ~0.3. For the CRISPR
526 dropout screen, one WT and two independent *PPM1D* mutant Cas9-expressing OCI-AML2 cell
527 lines were used as biological replicates, with three technical replicates per line. 3×10^7 cells were
528 transduced with the lentivirus library supernatant. Three days post-transduction, the cells were
529 selected with puromycin for three days. Cells were collected on day 28 for genomic DNA isolation
530 using isopropanol precipitation. Illumina adapters and barcodes were added to samples by PCR
531 as previously described (Tzelepis et al., 2016). Single-end sequencing was performed on the
532 HiSeq 2000 V4 platform and cell-essential genes were identified using the MaGECK-VISPR (Li
533 et al., 2014).
534
535 **Competitive Proliferation Assay**
536 Gene-specific sgRNAs were cloned into the pKLV2-U6gRNA5(BbsI)-PGKpuro2ABFP (Addgene
537 #67974) lentiviral backbone. 293T cells (0.4×10^6 cells per well) were seeded in a six-well plate
538 the day prior and transfected using lipofectamine 3000 with pMD2G (0.8 ug), pAX2 (1.6 ug), and
539 the sgRNA-BFP (1.6 ug) plasmids. Cas9-expressing cells were then seeded in 12-well plates
540 (200k cells per well, in triplicates) in media supplemented with 8ug/ml polybrene and 5 ug/mL
541 blasticidin, and lentivirally transduced at a titer that yields 50% infection efficiency. Cells were
542 assayed using flow cytometry for BFP expression between 4- and 16-days post-transduction and
543 normalized to the BFP percentage at day 4.
544
545 **Drug and Proliferation Assays**
546 Drug and proliferation assays were done using the Cell Proliferation MTT Kit (Sigma) as per
547 manufacturer's protocol. Briefly, 1×10^4 cells were plated in 96-well, flat bottom plates and treated
548 with vehicle or drugs in a total volume of 100 uL. Plates were incubated at 37ºC for at least 24
549 hours. 10 uL of MTT labeling reagent was added to each well and incubated for 4 hours. 100 uL

of solubilization buffer was added to each well and incubated overnight. Plates were analyzed using a fluorometric microplate reader at 550 nm. Stock solutions of ATN-224 (Cayman Chemical #23553) and LCS-1 (MedChem, HY-115445) were in DMSO and frozen in –20ºC.

SOD Activity Assay

SOD activity was measured per manufacturer's protocol (Invitrogen, Cat#EIASODC). Briefly, cells were treated with low or high-dose ATN-224 (0.625 uM and 1.25 uM, respectively) for 16-hours and harvested. Cells were washed with PBS and lysed with ice cold NP-40 lysis buffer (Invitrogen #FNN0021) with protease inhibitor (Thermofisher, #78440). Cells were sonicated for 5 seconds x 5 rounds and then spun at 13,000 rpm for 10 minutes at 4ºC. Protein concentrations were measured using BCA assay (Thermofisher, #23225) and diluted to a concentration of 10 ug/uL. 100 ug (10 uL) of protein was loaded per sample and incubated for 20 minutes with the added substrates. Plates were read on a microplate reader at 450 nm.

Intravenous transplantation of leukemia cells in NSG mice

WT and PPM1D-mutant OCI-AML2 cells were transduced with empty vector or sgSOD1 lentivirus, as described in the "Competitive Proliferation Assay" methods section above. Three days post-transduction, cells underwent puromycin selection (3 ug/mL). On day six post-transduction, the infection rate was determined by flow cytometry using the percentage of BFP+ cells. All samples had an infection rate of >95%. 8-week-old male NOD.Cg-*Prkdc*^{scid}*Il2rg*^{tm1Wjl}/SzJ (NSG) mice were purchased from The Jackson Laboratory (strain #005557) and sublethally irradiated (250 cGy) immediately prior to transplantation. 2 x 10^6 cells were intravenously injected in the tail vein of mice (n=8 per group). After transplantation, mice were monitored daily for disease progression and humane euthanasia was performed when animals lost >15% body weight or had signs of severe disease (limb paralysis, decreased activity, and hunching). All animal procedures and studies were done in accordance with the Institutional Animal Care and Use Committee (IACUC).

Alkaline Comet Assay

Comet assays were conducted as previously described (Greve et al., 2012; Schmezer et al., 2001). Cells were resuspended to 1 x 10^5 cells/mL and mixed with 1% low-melting agarose (R&D Systems) at a 1:10 ratio and plated on 2-well comet slides (R&D Systems). Cells were then lysed overnight and immersed in alkaline unwinding solution as per manufacturer's protocol (Trevigen). Fluorescence microscopy was performed at 10X magnification using the Keyence BZ-X800 microscope and analyses of comet tails were performed using the Comet Assay IV software (Instem). At least 150 comet tails were measured per sample.

Chromosome aberration analysis mitotic chromosome spreads

Primary resting mouse splenic B-cells were isolated using anti-CD43 microbeads (Miltenyi Biotec) and activated with 25 ug/mL LPS (Sigma), 5 ng/mL IL-4 (Sigma), and 0.5 ug/mL anti-CD180 (BD Pharmingen) for 30 hours. The cells were then treated with cisplatin for 16 hours at two concentrations - 0.5 uM and 5 uM cisplatin. Metaphases were prepared as previously described (Zong et al., 2019). Briefly, cells were arrested at mitosis with colcemid (0.1 ug/mL, ThermoFisher) for 1 hour. Cells were then incubated in a prewarmed, hypotonic solution of potassium chloride (75 mM) for 20 minutes to induce swelling and fixed in methanol/glacial acetic acid (3:1). Droplets

were spread onto glass slides inside a cytogenetic drying chamber. Fluorescence *in situ* hybridization was performed using a Cy3-labeled peptide nucleic acid probe to stain telomeres and DNA was counterstained by DAPI. At least 50 metaphases were scored for chromosome aberrations for each experimental group.

ROS Assays

To measure superoxide, total cellular reactive oxygen species (ROS), and lipid peroxidation, 1 x 10^6 cells were collected after the indicated treatments and washed with PBS. The cells were stained with 1 uM Mitosox Green (Thermofisher), 5 uM dihydroethidium (Thermofisher), 20 uM 2'7'-dichlorofluorescin diacetate (DCFDA, Abcam), or 2.5 uM BODIPY 581/591 (Thermofisher) in FBS-free Hanks' buffered saline solution (HBSS, Thermofisher), and incubated at 37ºC for 30 minutes. The staining was quenched with flow buffer (PBS, 2% FBS, 1% HEPES) and washed twice before resuspension in DAPI-containing flow buffer to assess ROS in viable cells. For detection of intracellular glutathione (GSH), we utilized the Intracellular glutathione detection assay kit (abcam) as per manufacturer's protocol. The data was acquired using an LSRII (BD Biosciences) and analyzed on Flowjo. The mean fluorescence intensity (MFI) was used for data analysis.

Reverse-Phase Protein Array

Reverse phase protein array assays for antibodies to proteins or phosphorylated proteins in different functional pathways were carried out as described previously (Coarfa et al., 2021; Lu H.-Y., 2021; Wang et al., 2022). Specifically, protein lysates were prepared from cultured cells with modified Tissue Protein Extraction Reagent (TPER) (Life Technologies Corporation, Carlsbad, CA) and a cocktail of protease and phosphatase inhibitors (Roche, Pleasanton, CA) (Lu et. al. 2021). The lysates were diluted into 0.5 mg/ml in SDS sample buffer and denatured on the same day. The Quanterix 2470 Arrayer (Quanterix, Billerica, MA) with a 40 pin (185 μm) configuration was used to spot samples and control lysates onto nitrocellulose-coated slides (Grace Bio-labs, Bend, OR) using an array format of 960 lysates/slide (2880 spots/slide). The slides were processed as described and probed with a set of 264 antibodies against total proteins and phosphoproteins using an automated slide stainer Autolink 48 (Dako, Santa Clara, CA). Each slide was incubated with one specific primary antibody and a negative control slide was incubated with antibody diluent without any primary antibody. Primary antibody binding was detected using a biotinylated secondary antibody followed by streptavidin-conjugated IRDye680 fluorophore (LI-COR Biosciences, Lincoln, NE). Total protein content of each spotted lysate was assessed by fluorescent staining with Sypro Ruby Protein Blot Stain according to the manufacturer's instructions (Molecular Probes, Eugene, OR).

Fluorescence-labeled slides were scanned on a GenePix 4400 AL scanner, along with accompanying negative control slides, at an appropriate PMT to obtain optimal signal for this specific set of samples. The images were analyzed with GenePix Pro 7.0 (Molecular Devices, Silicon Valley, CA). Total fluorescence signal intensities of each spot were obtained after subtraction of the local background signal for each slide and were then normalized for variation in total protein, background and non-specific labeling using a group-based normalization method as described (Lu H.-Y., 2021). For each spot on the array, the-background-subtracted foreground

signal intensity was subtracted by the corresponding signal intensity of the negative control slide (omission of primary antibody) and then normalized to the corresponding signal intensity of total protein for that spot. Each image, along with its normalized data, was evaluated for quality through manual inspection and control samples. Antibody slides that failed the quality inspection were either repeated at the end of the staining runs or removed before data reporting. A total of 261 antibodies remained in the list. Multiple t-tests with Benajimini Hochberg correction were performed for statistical analysis and filtering was based on an FDR <0.2 and linear fold change of >1.25.

RNA-sequencing

Bulk RNA-sequencing was performed on WT and *PPM1D*-mutant OCI-AML2 cells after lentiviral *SOD1* CRISPR knockout. Cells were transduced with pKLV2-U6-sgRNA-BFP lentivirus (either empty vector or with *SOD1*-sgRNA). Transduced cells were then cultured for 10 days and BFP+ cells were sorted directly into Buffer RLT Plus with ß-mercaptoethanol. RNA was isolated using the Allprep DNA/RNA Micro Kit (Qiagen) per manufacturer's protocols. RNA-sequencing library preparation was done using the True-Seq Stranded mRNA kit (Illumina) per manufacturer's protocol. Quality control of libraries was performed using a TapeStation D1000 ScreenTape (Agilent, 5067-5584). Libraries were then sequenced using an Illumina Nextseq 2000 sequencer, aiming for >20 million reads per biological replicate. Paired-end RNA-sequencing reads were obtained. obtained and trimmed using trimGalore (https://github.com/FelixKrueger/TrimGalore). Mapping was performed using the STAR package (Dobin et al., 2013) against the human genome build UCSC hg38 and counts were quantified with featureCounts (Liao et al., 2014). Differential expression analysis was performed using the DESeq2 R package (1.28.1) (Love et al., 2014). P-values were adjusted with Benjamini and Hochberg's approach for controlling the false discovery rate (FDR). Significant differentially expressed genes between the indicated comparisons were filtered based on an FDR<0.05 and absolute fold change exceeding 1.5. Pathway enrichment analysis was carried out using the GSEA (http://software.broadinstitute.org/gsea/index.jsp) software package and significance was achieved for adjust FDR<0.25.

Seahorse Assay

Mitochondrial bioenergetics in AML cell lines were performed using the Seahorse XFp Cell Mito Stress Kit (Agilent Technologies) on the Seahorse XFe96 Analyzer. Cells were resuspended in XF RPMI base media supplemented with 1 mM pyruvate, 2 mM L-glutamine, 10 mM glucose. 1 x 10^5 cells/well were seeded in poly-D-lysine (Thermofisher) coated XFe96 plates. The plate was incubated in a non-CO_2 incubator at 37ºC for 1 hour to equilibrate. OCR and ECAR measurements were taken at baseline and every 8 minutes after sequential addition of oligomycin (2 uM), FCCP (0.5 uM), and rotenone/ antimycin A (0.75 uM). All measurements were normalized to the number of viable cells.

Generation of *PPM1D* WT U2OS cells using CRISPR editing

U2OS cells containing the DR-GFP (for homologous recombination) or EJ5-GFP (for non-homologous end-joining) DNA repair reporter cassettes were kindly provided by the Bertuch Lab at Baylor College of Medicine. To establish *PPM1D*-WT isogenic lines, knock-in CRISPR editing was performed with a single-stranded oligodeoxynucleotide (ssODN) template: TGCCCTGGTTC

682 GTAGCAATGCCTTCTCAGAGAATTTTCTAGAGGTTTCAGCTGAGATAGCTCGTGAGAATGT
683 ACAAGGTGTAGTCATACCCTAAAAGATCCAGAACCACTTGAAGAAAATGCGCTAAAGCCCT
684 GACTTTAAGGATACA. The *PPM1D* sgRNA sequence used was: ATAGCTCGAGA
685 GAATGTCCA. 1.3 ug of Cas9 (IDT) was incubated with 1 ug of sgRNA for 15 minutes at room
686 temperature. 1 ug of the ssODN template was then added to the Cas9-sgRNA complexes and
687 mixed with 20,000 U2OS cells and resuspended in 10 uL of Buffer R, immediately prior to
688 electroporation. The neon electroporation system was used with the following conditions: 1400v,
689 15 ms, 4 pulses. Single cell-derived clones were genotyped by Sanger sequencing and PPM1D
690 protein expression was validated by western blot.
691
692 **GFP reporter-based DNA repair assays**
693 For the DNA repair reporter assay, 100,000 U2OS cells were seeded in a 12-well plate in
694 antibiotic-free Dulbecco's Modified Eagle Medium (DMEM, Thermofisher) supplemented with 10%
695 FBS. Cells were transfected with 3.6 uL of Lipofectamine 2000 (Invitrogen) in 200 uL of OptiMEM
696 with 0.8 ug of the I-SceI expression plasmid (pCBASce, Addgene #6096*0*). The media was
697 replaced the next morning and the cells were trypsinized 48-hours post-transfection for analysis
698 of GFP expression by flow cytometry (BD Biosciences).
699
700 **Immunofluorescence microscopy**
701 12 mm glass coverslips were coated with 50 ug/mL poly-D-lysine (Thermofisher) for 30 minutes
702 at room temperature and washed with sterile PBS. 0.5 x 10^6 suspension cells/well were seeded
703 on coverslips and incubated for 1 hour at 37ºC to allow for adherence. Samples were then fixed
704 with 4% paraformaldehyde for 10 minutes at 37ºC and washed three times with 0.01% Triton-X
705 PBS (PBS-T). Fixed cells were permeabilized with 0.5% PBS-T for 20 minutes, washed three
706 times, and incubated with 5% goat serum (Thermofisher) for 1 hour at room temperature.
707 Afterwards, samples were incubated overnight at 4ºC with the following primary antibodies: rabbit
708 anti-Rad51 (Cell Signaling #8875S 1:100) or rabbit anti-53BP1 (ThermoFisher #PA1-16565,
709 1:500). The following day, samples were washed and incubated at room temperature for 1 hour
710 with Alexafluor 488-conjugated goat anti-rabbit IgG (#111-545-144, Jackson ImmunoResearch,
711 1:500). After secondary antibody incubation, the coverslips were washed three times with PBS
712 and mounted with fluoromount-G mounting medium with DAPI (Thermofisher) on glass
713 microscope slides and sealed with nail polish. Imaging was done on the Keyence BZ-X800
714 microscope and foci analysis was performed using CellProfiler.
715
716 **Immunoblotting**
717 Cells were lysed with 1x RIPA buffer supplemented with Halt Protease and Phosphatase inhibitor
718 cocktail (Thermofisher) for 1 hour at 4ºC. Protein concentration was quantified using the Pierce
719 BCA protein assay kit (Thermofisher) and boiled at 95ºC in 1x Laemmli (Biorad) for 7 minutes.
720 The samples in which mitochondrial proteins were probed were not boiled, as boiling can cause
721 signal reduction. Instead, samples were warmed to 37ºC for 30 minutes prior to loading. The
722 proteins were separated by SDS-PAGE on 4-15% gradient gels (Biorad) and transferred on to
723 PVDF membranes using the iBlot Dry Blotting system (Thermofisher). Membranes were
724 incubated for 1 hour at room temperature in 5% milk in Tris-buffered saline solution with Tween-
725 20 (TBST). After washing, the membranes were incubated overnight at 4ºC with the following

primary antibodies: mouse anti-PPM1D (F-10, Santa Cruz, 1:1000), mouse anti-GAPDH (MAB374, Millipore, 1:200), mouse total OXPHOS Human antibody cocktail (ab110411, Abcam, 1:1000), mouse anti-Vinculin (V9131, Sigma Aldrich, 1:2000). The following day, membranes were washed twice with TBST and incubated for 1 hour with HRP-linked anti-rabbit IgG or anti-mouse IgG (Cell Signaling, 1:5000 – 1:10,000) at room temperature. Blots were imaged on the Bio-Rad ChemiDoc platform.

Statistical analysis

Statistical analysis incorporated in the MaGECK-VISPR algorithm includes p-value and FDR calculations. GraphPad Prism 6.0 was used for other statistical analyses. The sample size (n) specified in the Figure Legends was used for statistical analysis and denotes the number of independent biological replicates. The main conclusions were supported by data obtained from at least two biological replicates. The graphs presented in the figures are shown with error bars indicating either mean ± SEM or mean ± SD, as mentioned in the Figure Legends. Two-tailed t-tests were performed to calculate statistics, assuming unequal standard deviations, unless mentioned otherwise. Significance levels are indicated in the figures and were determined using GraphPad PRISM. Results were considered statistically significant at *$p<0.05$, **$p<0.01$, ***$p<0.001$, ****$p<0.0001$.

Acknowledgments

This work was supported by R01CA237291 and P01CA265748. This work was also supported by the NCI Cancer Center Support Grant P30CA125123 which partly supports the Cytometry Core, the Proteomics & Metabolomics Core, and the Antibody-based Proteomics Core. Support for the cores was also provided by the Cancer Prevention and Research Institute of Texas (CPRIT) from grants: RP180672, RR024574, and RP210227 and NIH S10OD028648. LZ was supported by the Baylor Research Advocates for Student Scientists (BRASS) Foundation, and the Janice McNair Medical Foundation.

Author Contributions:

Conceptualization: LZ, JIH, SMW, AT, AN, JNA, KT, GV, MAG
Methodology: LZ, JIH, EDB, CWC, AT, RM, RR, SJ, LV, BBadV
Investigation: LZ, JIH, EDB, CWC, AGG, AGM, SMW, EC, RM, RR, AN, SJ, SH, JNA
Visualization: LZ, EC, TJP, SMW
Computational analysis: EDB, CWC, TDP
Supervision: JIH, AN, BBAdV, CC, JNA, KT, GV, MAG
Writing—original draft: LZ, JIH
Writing—review & editing: LZ, JIH, EDB, GV, SMW, CWC, AT, MAG,
Contributed unpublished, essential data, or reagents: KT, HU, AGG, AGM, RM, RR, JNA

Competing Interests: The authors declare they have no competing interests.

Data and materials availability: All data are available in the main text or in the supplementary materials. All raw and processed data generated in this work will be publicly available at GEO data repositor pending scientific review. The human cell lines generated by the Goodell laboratory for this study are available upon request and will require a standard Materials Transfer Agreement (MTA). Any additional information required to analyze the data reported in this paper is available from the lead contact upon request.

References

Abati, E., Bresolin, N., Comi, G., and Corti, S. (2020). Silence superoxide dismutase 1 (SOD1): a promising therapeutic target for amyotrophic lateral sclerosis (ALS). Expert Opin Ther Targets *24*, 295-310.

Ali, A.Y., Abedini, M.R., and Tsang, B.K. (2012). The oncogenic phosphatase PPM1D confers cisplatin resistance in ovarian carcinoma cells by attenuating checkpoint kinase 1 and p53 activation. Oncogene *31*, 2175-2186.

Bar, O., Ebenau, L., Weiner, K., Mintz, M., and Boles, R.G. (2023). Whole exome/genome sequencing in cyclic vomiting syndrome reveals multiple candidate genes, suggesting a model of elevated intracellular cations and mitochondrial dysfunction. Front Neurol *14*, 1151835.

Bolton, K.L., Ptashkin, R.N., Gao, T., Braunstein, L., Devlin, S.M., Kelly, D., Patel, M., Berthon, A., Syed, A., Yabe, M.*, et al.* (2020). Cancer therapy shapes the fitness landscape of clonal hematopoiesis. Nat Genet *52*, 1219-1226.

Bulavin, D.V., Demidov, O.N., Saito, S., Kauraniemi, P., Phillips, C., Amundson, S.A., Ambrosino, C., Sauter, G., Nebreda, A.R., Anderson, C.W.*, et al.* (2002). Amplification of PPM1D in human tumors abrogates p53 tumor-suppressor activity. Nat Genet *31*, 210-215.

Burdova, K., Storchova, R., Palek, M., and Macurek, L. (2019). WIP1 Promotes Homologous Recombination and Modulates Sensitivity to PARP Inhibitors. Cells *8*.

Cappelli, E., Cuccarolo, P., Stroppiana, G., Miano, M., Bottega, R., Cossu, V., Degan, P., and Ravera, S. (2017). Defects in mitochondrial energetic function compels Fanconi Anaemia cells to glycolytic metabolism. Biochim Biophys Acta Mol Basis Dis *1863*, 1214-1221.

Ceccaldi, R., Sarangi, P., and D'Andrea, A.D. (2016). The Fanconi anaemia pathway: new players and new functions. Nat Rev Mol Cell Biol *17*, 337-349.

Cha, H., Lowe, J.M., Li, H., Lee, J.S., Belova, G.I., Bulavin, D.V., and Fornace, A.J., Jr. (2010). Wip1 directly dephosphorylates gamma-H2AX and attenuates the DNA damage response. Cancer Res *70*, 4112-4122.

Chidambaram, M.V., Barnes, G., and Frieden, E. (1984). Inhibition of ceruloplasmin and other copper oxidases by thiomolybdate. J Inorg Biochem *22*, 231-240.

Ciccia, A., and Elledge, S.J. (2010). The DNA damage response: making it safe to play with knives. Mol Cell *40*, 179-204.

Coarfa, C., Grimm, S.L., Rajapakshe, K., Perera, D., Lu, H.Y., Wang, X., Christensen, K.R., Mo, Q., Edwards, D.P., and Huang, S. (2021). Reverse-Phase Protein Array: Technology, Application, Data Processing, and Integration. J Biomol Tech.

Dhar, S.K., Tangpong, J., Chaiswing, L., Oberley, T.D., and St Clair, D.K. (2011). Manganese superoxide dismutase is a p53-regulated gene that switches cancers between early and advanced stages. Cancer Res *71*, 6684-6695.

Dobin, A., Davis, C.A., Schlesinger, F., Drenkow, J., Zaleski, C., Jha, S., Batut, P., Chaisson, M., and Gingeras, T.R. (2013). STAR: ultrafast universal RNA-seq aligner. Bioinformatics *29*, 15-21.

Fiscella, M., Zhang, H., Fan, S., Sakaguchi, K., Shen, S., Mercer, W.E., Vande Woude, G.F., O'Connor, P.M., and Appella, E. (1997). Wip1, a novel human protein phosphatase that is induced in response to ionizing radiation in a p53-dependent manner. Proc Natl Acad Sci U S A *94*, 6048-6053.

Fu, Z., Sun, G., and Gu, T. (2014). Proto-oncogene Wip1, a member of a new family of proliferative genes in NSCLC and its clinical significance. Tumour Biol *35*, 2975-2981.

Genovese, G., Kahler, A.K., Handsaker, R.E., Lindberg, J., Rose, S.A., Bakhoum, S.F., Chambert, K., Mick, E., Neale, B.M., Fromer, M.*, et al.* (2014). Clonal hematopoiesis and blood-cancer risk inferred from blood DNA sequence. N Engl J Med *371*, 2477-2487.

821 Gnugge, R., and Symington, L.S. (2021). DNA end resection during homologous recombination.
822 Curr Opin Genet Dev *71*, 99-105.
823 Greve, B., Bolling, T., Amler, S., Rossler, U., Gomolka, M., Mayer, C., Popanda, O., Dreffke, K.,
824 Rickinger, A., Fritz, E.*, et al.* (2012). Evaluation of different biomarkers to predict individual
825 radiosensitivity in an inter-laboratory comparison--lessons for future studies. PLoS One *7*,
826 e47185.
827 Guleria, A., and Chandna, S. (2016). ATM kinase: Much more than a DNA damage responsive
828 protein. DNA Repair (Amst) *39*, 1-20.
829 Hanahan, D., and Weinberg, R.A. (2011). Hallmarks of cancer: the next generation. Cell *144*,
830 646-674.
831 Harper, J.W., Adami, G.R., Wei, N., Keyomarsi, K., and Elledge, S.J. (1993). The p21 Cdk-
832 interacting protein Cip1 is a potent inhibitor of G1 cyclin-dependent kinases. Cell *75*, 805-
833 816.
834 Hawash, M., Jaradat, N., Abualhasan, M., Thaher, M., Sawalhi, R., Younes, N., Shanaa, A.,
835 Nuseirat, M., and Mousa, A. (2022). In vitro and in vivo assessment of the antioxidant
836 potential of isoxazole derivatives. Sci Rep *12*, 18223.
837 He, X.L., Xiao, Q., Zhou, Z.P., and Hui, C.Y. (2021). PPM1D accelerates proliferation and
838 metastasis of osteosarcoma by activating PKP2. Eur Rev Med Pharmacol Sci *25*, 78-85.
839 Hoeijmakers, J.H. (2009). DNA damage, aging, and cancer. N Engl J Med *361*, 1475-1485.
840 Hsu, J.I., Dayaram, T., Tovy, A., De Braekeleer, E., Jeong, M., Wang, F., Zhang, J., Heffernan,
841 T.P., Gera, S., Kovacs, J.J.*, et al.* (2018). PPM1D Mutations Drive Clonal Hematopoiesis
842 in Response to Cytotoxic Chemotherapy. Cell Stem Cell *23*, 700-713 e706.
843 Huang, P., Feng, L., Oldham, E.A., Keating, M.J., and Plunkett, W. (2000). Superoxide dismutase
844 as a target for the selective killing of cancer cells. Nature *407*, 390-395.
845 Jaiswal, S., Fontanillas, P., Flannick, J., Manning, A., Grauman, P.V., Mar, B.G., Lindsley, R.C.,
846 Mermel, C.H., Burtt, N., Chavez, A.*, et al.* (2014). Age-related clonal hematopoiesis
847 associated with adverse outcomes. N Engl J Med *371*, 2488-2498.
848 Jansen, S., Geuer, S., Pfundt, R., Brough, R., Ghongane, P., Herkert, J.C., Marco, E.J.,
849 Willemsen, M.H., Kleefstra, T., Hannibal, M.*, et al.* (2017). De Novo Truncating Mutations
850 in the Last and Penultimate Exons of PPM1D Cause an Intellectual Disability Syndrome.
851 Am J Hum Genet *100*, 650-658.
852 Jiao, L., Shen, D., Liu, G., Jia, J., Geng, J., Wang, H., and Sun, Y. (2014). PPM1D as a novel
853 biomarker for prostate cancer after radical prostatectomy. Anticancer Res *34*, 2919-2925.
854 Juarez, J.C., Betancourt, O., Jr., Pirie-Shepherd, S.R., Guan, X., Price, M.L., Shaw, D.E., Mazar,
855 A.P., and Donate, F. (2006). Copper binding by tetrathiomolybdate attenuates
856 angiogenesis and tumor cell proliferation through the inhibition of superoxide dismutase 1.
857 Clin Cancer Res *12*, 4974-4982.
858 Kahn, J.D., Miller, P.G., Silver, A.J., Sellar, R.S., Bhatt, S., Gibson, C., McConkey, M., Adams,
859 D., Mar, B., Mertins, P.*, et al.* (2018). PPM1D-truncating mutations confer resistance to
860 chemotherapy and sensitivity to PPM1D inhibition in hematopoietic cells. Blood *132*, 1095-
861 1105.
862 Kang, M.Y., Kim, H.B., Piao, C., Lee, K.H., Hyun, J.W., Chang, I.Y., and You, H.J. (2013). The
863 critical role of catalase in prooxidant and antioxidant function of p53. Cell Death Differ *20*,
864 117-129.
865 Khadka, P., Reitman, Z.J., Lu, S., Buchan, G., Gionet, G., Dubois, F., Carvalho, D.M., Shih, J.,
866 Zhang, S., Greenwald, N.F.*, et al.* (2022). PPM1D mutations are oncogenic drivers of de
867 novo diffuse midline glioma formation. Nat Commun *13*, 604.
868 Kleiblova, P., Shaltiel, I.A., Benada, J., Sevcik, J., Pechackova, S., Pohlreich, P., Voest, E.E.,
869 Dundr, P., Bartek, J., Kleibl, Z.*, et al.* (2013). Gain-of-function mutations of PPM1D/Wip1
870 impair the p53-dependent G1 checkpoint. J Cell Biol *201*, 511-521.

871 Korkina, L.G., Samochatova, E.V., Maschan, A.A., Suslova, T.B., Cheremisina, Z.P., and
872 Afanas'ev, I.B. (1992). Release of active oxygen radicals by leukocytes of Fanconi anemia
873 patients. J Leukoc Biol *52*, 357-362.
874 Kottemann, M.C., and Smogorzewska, A. (2013). Fanconi anaemia and the repair of Watson and
875 Crick DNA crosslinks. Nature *493*, 356-363.
876 Kumari, U., Ya Jun, W., Huat Bay, B., and Lyakhovich, A. (2014). Evidence of mitochondrial
877 dysfunction and impaired ROS detoxifying machinery in Fanconi anemia cells. Oncogene
878 *33*, 165-172.
879 Lambros, M.B., Natrajan, R., Geyer, F.C., Lopez-Garcia, M.A., Dedes, K.J., Savage, K., Lacroix-
880 Triki, M., Jones, R.L., Lord, C.J., Linardopoulos, S.*, et al.* (2010). PPM1D gene
881 amplification and overexpression in breast cancer: a qRT-PCR and chromogenic in situ
882 hybridization study. Mod Pathol *23*, 1334-1345.
883 Lee, K., Briehl, M.M., Mazar, A.P., Batinic-Haberle, I., Reboucas, J.S., Glinsmann-Gibson, B.,
884 Rimsza, L.M., and Tome, M.E. (2013). The copper chelator ATN-224 induces peroxynitrite-
885 dependent cell death in hematological malignancies. Free Radic Biol Med *60*, 157-167.
886 Li, B., Hu, J., He, D., Chen, Q., Liu, S., Zhu, X., and Yu, M. (2020a). PPM1D Knockdown
887 Suppresses Cell Proliferation, Promotes Cell Apoptosis, and Activates p38 MAPK/p53
888 Signaling Pathway in Acute Myeloid Leukemia. Technol Cancer Res Treat *19*,
889 1533033820942312.
890 Li, J., Yang, Y., Peng, Y., Austin, R.J., van Eyndhoven, W.G., Nguyen, K.C., Gabriele, T.,
891 McCurrach, M.E., Marks, J.R., Hoey, T.*, et al.* (2002). Oncogenic properties of PPM1D
892 located within a breast cancer amplification epicenter at 17q23. Nat Genet *31*, 133-134.
893 Li, K., Liu, Y., Xu, S., and Wang, J. (2020b). PPM1D Functions as Oncogene and is Associated
894 with Poor Prognosis in Esophageal Squamous Cell Carcinoma. Pathol Oncol Res *26*, 387-
895 395.
896 Li, W., Xu, H., Xiao, T., Cong, L., Love, M.I., Zhang, F., Irizarry, R.A., Liu, J.S., Brown, M., and
897 Liu, X.S. (2014). MAGeCK enables robust identification of essential genes from genome-
898 scale CRISPR/Cas9 knockout screens. Genome Biol *15*, 554.
899 Li, Y., Fang, M., Xu, Z., and Li, X. (2022). Tetrathiomolybdate as an old drug in a new use: As a
900 chemotherapeutic sensitizer for non-small cell lung cancer. J Inorg Biochem *233*, 111865.
901 Liang, Y., Liu, J., and Feng, Z. (2013). The regulation of cellular metabolism by tumor suppressor
902 p53. Cell Biosci *3*, 9.
903 Liao, Y., Smyth, G.K., and Shi, W. (2014). featureCounts: an efficient general purpose program
904 for assigning sequence reads to genomic features. Bioinformatics *30*, 923-930.
905 Lin, J., Zahurak, M., Beer, T.M., Ryan, C.J., Wilding, G., Mathew, P., Morris, M., Callahan, J.A.,
906 Gordon, G., Reich, S.D.*, et al.* (2013). A non-comparative randomized phase II study of 2
907 doses of ATN-224, a copper/zinc superoxide dismutase inhibitor, in patients with
908 biochemically recurrent hormone-naive prostate cancer. Urol Oncol *31*, 581-588.
909 Lindsley, R.C., Saber, W., Mar, B.G., Redd, R., Wang, T., Haagenson, M.D., Grauman, P.V., Hu,
910 Z.H., Spellman, S.R., Lee, S.J.*, et al.* (2017). Prognostic Mutations in Myelodysplastic
911 Syndrome after Stem-Cell Transplantation. N Engl J Med *376*, 536-547.
912 Ling, M., Liu, Q., Wang, Y., Liu, X., Jiang, M., and Hu, J. (2022). LCS-1 inhibition of superoxide
913 dismutase 1 induces ROS-dependent death of glioma cells and degradates PARP and
914 BRCA1. Front Oncol *12*, 937444.
915 Love, M.I., Huber, W., and Anders, S. (2014). Moderated estimation of fold change and dispersion
916 for RNA-seq data with DESeq2. Genome Biol *15*, 550.
917 Lowndes, S.A., Adams, A., Timms, A., Fisher, N., Smythe, J., Watt, S.M., Joel, S., Donate, F.,
918 Hayward, C., Reich, S.*, et al.* (2008). Phase I study of copper-binding agent ATN-224 in
919 patients with advanced solid tumors. Clin Cancer Res *14*, 7526-7534.
920 Lowndes, S.A., Sheldon, H.V., Cai, S., Taylor, J.M., and Harris, A.L. (2009). Copper chelator
921 ATN-224 inhibits endothelial function by multiple mechanisms. Microvasc Res *77*, 314-326.

Lu H.-Y., X.J., Perera D.N., Rajapakshe K., Wang X., Costello M., Holloway K.R., Ramos C., Grimm S.L., Julia Wulfkuhle, Coarfa C, Edwards D.P., Zhu M.X., Huang S. (2021). High-Throughput Evaluation of Metabolic Activities Using Reverse Phase Protein Array Technology. In Neuron Signaling in Metabolic Regulation (Boca Raton: CRC Press), p. 25.

Lu, X., Nannenga, B., and Donehower, L.A. (2005). PPM1D dephosphorylates Chk1 and p53 and abrogates cell cycle checkpoints. Genes Dev *19*, 1162-1174.

Maya-Mendoza, A., Ostrakova, J., Kosar, M., Hall, A., Duskova, P., Mistrik, M., Merchut-Maya, J.M., Hodny, Z., Bartkova, J., Christensen, C.*, et al.* (2015). Myc and Ras oncogenes engage different energy metabolism programs and evoke distinct patterns of oxidative and DNA replication stress. Mol Oncol *9*, 601-616.

Miller, P.G., Sathappa, M., Moroco, J.A., Jiang, W., Qian, Y., Iqbal, S., Guo, Q., Giacomelli, A.O., Shaw, S., Vernier, C.*, et al.* (2022). Allosteric inhibition of PPM1D serine/threonine phosphatase via an altered conformational state. Nat Commun *13*, 3778.

Nguyen, T.A., Slattery, S.D., Moon, S.H., Darlington, Y.F., Lu, X., and Donehower, L.A. (2010). The oncogenic phosphatase WIP1 negatively regulates nucleotide excision repair. DNA Repair (Amst) *9*, 813-823.

Oliva-Trastoy, M., Berthonaud, V., Chevalier, A., Ducrot, C., Marsolier-Kergoat, M.C., Mann, C., and Leteurtre, F. (2007). The Wip1 phosphatase (PPM1D) antagonizes activation of the Chk2 tumour suppressor kinase. Oncogene *26*, 1449-1458.

Pagano, G., Talamanca, A.A., Castello, G., d'Ischia, M., Pallardo, F.V., Petrovic, S., Porto, B., Tiano, L., and Zatterale, A. (2013). Bone marrow cell transcripts from Fanconi anaemia patients reveal in vivo alterations in mitochondrial, redox and DNA repair pathways. Eur J Haematol *91*, 141-151.

Park, M.T., Kim, M.J., Suh, Y., Kim, R.K., Kim, H., Lim, E.J., Yoo, K.C., Lee, G.H., Kim, Y.H., Hwang, S.G.*, et al.* (2014). Novel signaling axis for ROS generation during K-Ras-induced cellular transformation. Cell Death Differ *21*, 1185-1197.

Peng, B., Wang, J., Hu, Y., Zhao, H., Hou, W., Zhao, H., Wang, H., Liao, J., and Xu, X. (2015). Modulation of LSD1 phosphorylation by CK2/WIP1 regulates RNF168-dependent 53BP1 recruitment in response to DNA damage. Nucleic Acids Res *43*, 5936-5947.

Peng, T.S., He, Y.H., Nie, T., Hu, X.D., Lu, H.Y., Yi, J., Shuai, Y.F., and Luo, M. (2014). PPM1D is a prognostic marker and therapeutic target in colorectal cancer. Exp Ther Med *8*, 430-434.

Peuget, S., Bonacci, T., Soubeyran, P., Iovanna, J., and Dusetti, N.J. (2014). Oxidative stress-induced p53 activity is enhanced by a redox-sensitive TP53INP1 SUMOylation. Cell Death Differ *21*, 1107-1118.

Poole, L.B. (2015). The basics of thiols and cysteines in redox biology and chemistry. Free Radic Biol Med *80*, 148-157.

Ruark, E., Snape, K., Humburg, P., Loveday, C., Bajrami, I., Brough, R., Rodrigues, D.N., Renwick, A., Seal, S., Ramsay, E.*, et al.* (2013). Mosaic PPM1D mutations are associated with predisposition to breast and ovarian cancer. Nature *493*, 406-410.

Sablina, A.A., Budanov, A.V., Ilyinskaya, G.V., Agapova, L.S., Kravchenko, J.E., and Chumakov, P.M. (2005). The antioxidant function of the p53 tumor suppressor. Nat Med *11*, 1306-1313.

Sajesh, B.V., Bailey, M., Lichtensztejn, Z., Hieter, P., and McManus, K.J. (2013). Synthetic lethal targeting of superoxide dismutase 1 selectively kills RAD54B-deficient colorectal cancer cells. Genetics *195*, 757-767.

Sajesh, B.V., and McManus, K.J. (2015). Targeting SOD1 induces synthetic lethal killing in BLM- and CHEK2-deficient colorectal cancer cells. Oncotarget *6*, 27907-27922.

Sauer, H., Wartenberg, M., and Hescheler, J. (2001). Reactive oxygen species as intracellular messengers during cell growth and differentiation. Cell Physiol Biochem *11*, 173-186.

Schmezer, P., Rajaee-Behbahani, N., Risch, A., Thiel, S., Rittgen, W., Drings, P., Dienemann, H., Kayser, K.W., Schulz, V., and Bartsch, H. (2001). Rapid screening assay for mutagen

973 sensitivity and DNA repair capacity in human peripheral blood lymphocytes. Mutagenesis
974 *16*, 25-30.
975 Sies, H., and Jones, D.P. (2020). Reactive oxygen species (ROS) as pleiotropic physiological
976 signalling agents. Nat Rev Mol Cell Biol *21*, 363-383.
977 Somwar, R., Erdjument-Bromage, H., Larsson, E., Shum, D., Lockwood, W.W., Yang, G., Sander,
978 C., Ouerfelli, O., Tempst, P.J., Djaballah, H.*, et al.* (2011). Superoxide dismutase 1 (SOD1)
979 is a target for a small molecule identified in a screen for inhibitors of the growth of lung
980 adenocarcinoma cell lines. Proc Natl Acad Sci U S A *108*, 16375-16380.
981 Steverding, D., and Barcelos, Y. (2020). Cytotoxic Activity of LCS-1 is not Only due to Inhibition
982 of SOD1. Drug Res (Stuttg) *70*, 57-60.
983 Sumpter, R., Jr., Sirasanagandla, S., Fernandez, A.F., Wei, Y., Dong, X., Franco, L., Zou, Z.,
984 Marchal, C., Lee, M.Y., Clapp, D.W.*, et al.* (2016). Fanconi Anemia Proteins Function in
985 Mitophagy and Immunity. Cell *165*, 867-881.
986 Takekawa, M., Adachi, M., Nakahata, A., Nakayama, I., Itoh, F., Tsukuda, H., Taya, Y., and Imai,
987 K. (2000). p53-inducible wip1 phosphatase mediates a negative feedback regulation of p38
988 MAPK-p53 signaling in response to UV radiation. EMBO J *19*, 6517-6526.
989 Tan, M., Li, S., Swaroop, M., Guan, K., Oberley, L.W., and Sun, Y. (1999). Transcriptional
990 activation of the human glutathione peroxidase promoter by p53. J Biol Chem *274*, 12061-
991 12066.
992 Thannickal, V.J., and Fanburg, B.L. (2000). Reactive oxygen species in cell signaling. Am J
993 Physiol Lung Cell Mol Physiol *279*, L1005-1028.
994 Tokheim, C., Wang, X., Timms, R.T., Zhang, B., Mena, E.L., Wang, B., Chen, C., Ge, J., Chu, J.,
995 Zhang, W.*, et al.* (2021). Systematic characterization of mutations altering protein
996 degradation in human cancers. Mol Cell *81*, 1292-1308 e1211.
997 Turrens, J.F. (2003). Mitochondrial formation of reactive oxygen species. Journal of Physiology
998 *552*, 335-344.
999 Tzelepis, K., Koike-Yusa, H., De Braekeleer, E., Li, Y., Metzakopian, E., Dovey, O.M., Mupo, A.,
1000 Grinkevich, V., Li, M., Mazan, M.*, et al.* (2016). A CRISPR Dropout Screen Identifies
1001 Genetic Vulnerabilities and Therapeutic Targets in Acute Myeloid Leukemia. Cell Rep *17*,
1002 1193-1205.
1003 Valentin-Vega, Y.A., Maclean, K.H., Tait-Mulder, J., Milasta, S., Steeves, M., Dorsey, F.C.,
1004 Cleveland, J.L., Green, D.R., and Kastan, M.B. (2012). Mitochondrial dysfunction in ataxia-
1005 telangiectasia. Blood *119*, 1490-1500.
1006 Wallace, D.C. (2005). A mitochondrial paradigm of metabolic and degenerative diseases, aging,
1007 and cancer: a dawn for evolutionary medicine. Annu Rev Genet *39*, 359-407.
1008 Wang, P., Rao, J., Yang, H., Zhao, H., and Yang, L. (2011). PPM1D silencing by lentiviral-
1009 mediated RNA interference inhibits proliferation and invasion of human glioma cells. J
1010 Huazhong Univ Sci Technolog Med Sci *31*, 94-99.
1011 Wang, X., Shi, Z., Lu, H.Y., Kim, J.J., Bu, W., Villalobos, J.A., Perera, D.N., Jung, S.Y., Wang, T.,
1012 Grimm, S.L.*, et al.* (2022). High-throughput profiling of histone post-translational
1013 modifications and chromatin modifying proteins by reverse phase protein array. J
1014 Proteomics *262*, 104596.
1015 Weinstock, D.M., Nakanishi, K., Helgadottir, H.R., and Jasin, M. (2006). Assaying double-strand
1016 break repair pathway choice in mammalian cells using a targeted endonuclease or the RAG
1017 recombinase. Methods Enzymol *409*, 524-540.
1018 Wojcik, M.H., Srivastava, S., Agrawal, P.B., Balci, T.B., Callewaert, B., Calvo, P.L., Carli, D.,
1019 Caudle, M., Colaiacovo, S., Cross, L.*, et al.* (2023). Jansen-de Vries syndrome: Expansion
1020 of the PPM1D clinical and phenotypic spectrum in 34 families. Am J Med Genet A.
1021 Wu, B., Guo, B.M., Kang, J., Deng, X.Z., Fan, Y.B., Zhang, X.P., and Ai, K.X. (2016). PPM1D
1022 exerts its oncogenic properties in human pancreatic cancer through multiple mechanisms.
1023 Apoptosis *21*, 365-378.

1024 Xu, Y., and Xu, D. (2020). Repair pathway choice for double-strand breaks. Essays Biochem *64*,
1025 765-777.
1026 Yin, H., Yan, Z., Liang, Y., Liu, B., and Su, Q. (2013). Knockdown of protein phosphatase
1027 magnesium-dependent 1 (PPM1D) through lentivirus-mediated RNA silencing inhibits
1028 colorectal carcinoma cell proliferation. Technol Cancer Res Treat *12*, 537-543.
1029 Yokoyama, A., Kakiuchi, N., Yoshizato, T., Nannya, Y., Suzuki, H., Takeuchi, Y., Shiozawa, Y.,
1030 Sato, Y., Aoki, K., Kim, S.K.*, et al.* (2019). Age-related remodelling of oesophageal epithelia
1031 by mutated cancer drivers. Nature *565*, 312-317.
1032 Yonish-Rouach, E., Resnitzky, D., Lotem, J., Sachs, L., Kimchi, A., and Oren, M. (1991). Wild-
1033 type p53 induces apoptosis of myeloid leukaemic cells that is inhibited by interleukin-6.
1034 Nature *352*, 345-347.
1035 Zhang, L., Chen, L.H., Wan, H., Yang, R., Wang, Z., Feng, J., Yang, S., Jones, S., Wang, S.,
1036 Zhou, W.*, et al.* (2014). Exome sequencing identifies somatic gain-of-function PPM1D
1037 mutations in brainstem gliomas. Nat Genet *46*, 726-730.
1038 Zong, D., Adam, S., Wang, Y., Sasanuma, H., Callen, E., Murga, M., Day, A., Kruhlak, M.J., Wong,
1039 N., Munro, M.*, et al.* (2019). BRCA1 Haploinsufficiency Is Masked by RNF168-Mediated
1040 Chromatin Ubiquitylation. Mol Cell *73*, 1267-1281 e1267.

1041

Figure 1

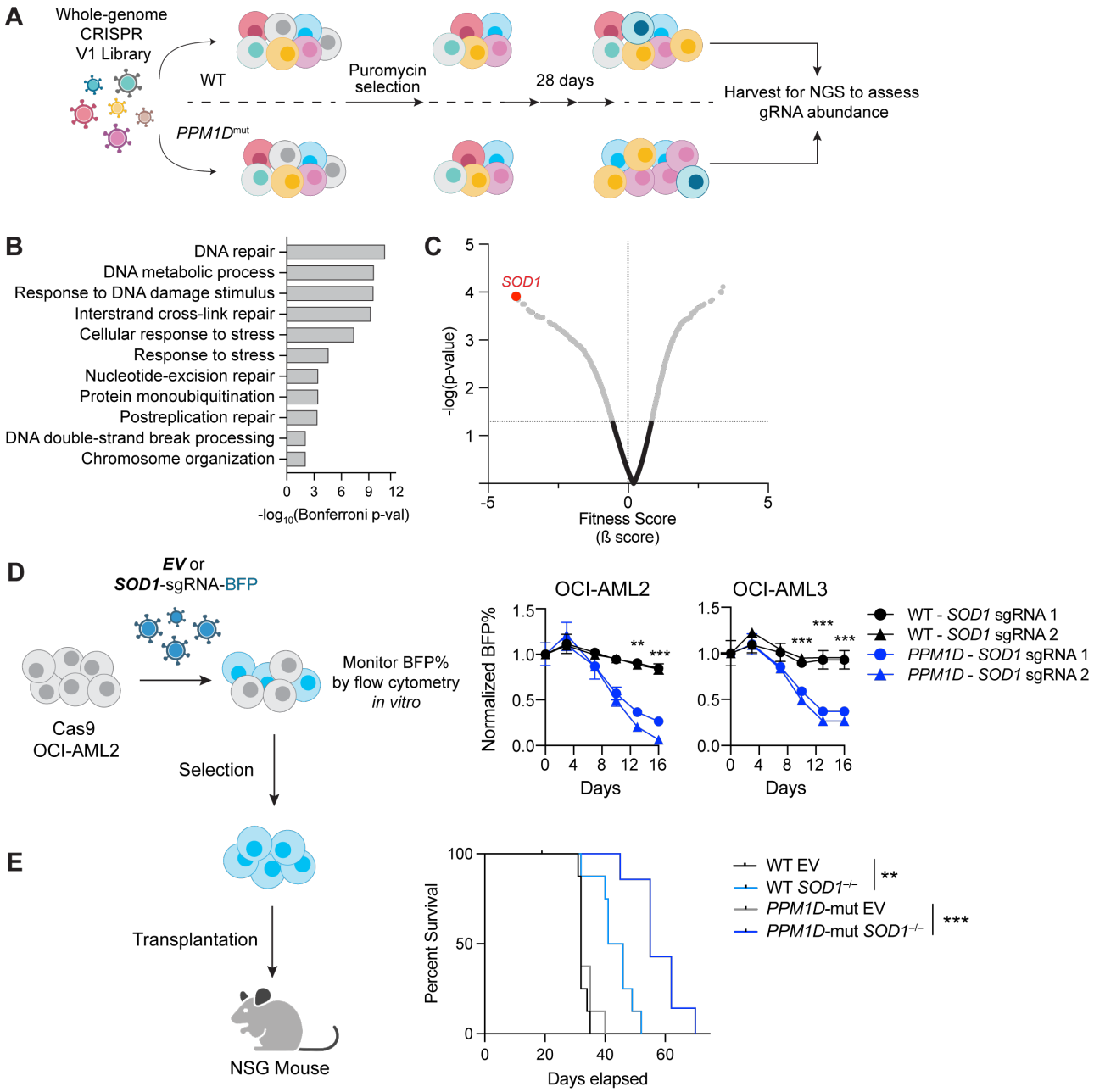

1042

1043 **Figure 1. *SOD1* is a synthetic lethal vulnerability of *PPM1D*-mutant leukemia cells.**
1044 **(A)** Schematic of whole-genome CRISPR dropout screen. WT Cas9-expressing OCI-AML2 and
1045 two isogenic *PPM1D*-mutant lines were transduced with the Human Improved Whole Genome
1046 Knockout CRISPR library V1 containing 90,709 guide RNAs (gRNAs) targeting 18,010 human
1047 genes at low multiplicity of infection (MOI~0.3). Each condition was performed in technical
1048 triplicates. Three days post-transduction, cells underwent puromycin selection for three days.
1049 Cells were harvested at day 10 as the initial timepoint and then harvested every three days
1050 afterwards. sgRNA sequencing was performed on cells collected on day 28. **(B)** Top biological
1051 processes based on gene ontology analysis of the top 37 genes essential for *PPM1D*-mutant cell
1052 survival. Enrichment and depletion of guides and genes were analyzed using MAGeCK-VISPR
1053 by comparing read counts from each *PPM1D*-mutant cell line replicate with counts from the initial
1054 starting population at day ten. **(C)** Volcano plot of synthetic lethal hits ranked by fitness score with
1055 a negative score indicating genes for which their knockout leads to decreased growth or survival.
1056 *SOD1* (highlighted) was the top hit from the screen. **(D)** Left: Schematic of competitive
1057 proliferation assays used for validation of CRISPR targets. Right: WT and *PPM1D*-mutant Cas9-
1058 OCI-AML2 and Cas9-OCI-AML3 cells were transduced with lentiviruses containing a single
1059 *SOD1*-gRNA with a blue fluorescent protein (BFP) reporter. Cells were assayed by flow cytometry
1060 every 3-4 days and normalized to the BFP percentage at day 3 post-transduction. Two unique
1061 gRNAs against *SOD1* were used per cell line and each condition was performed in technical
1062 duplicates; multiple unpaired t-tests, **$p<0.01$, ***$p<0.001$. **E)** Left: Cas9-expressing WT and
1063 *PPM1D*-mutant cells were transduced with control or sg*SOD1*-containing lentiviruses and
1064 underwent puromycin (3 ug/mL) selection for three days prior to transplantation. Sublethally-
1065 irradiated (250 cGy) NSG mice were intravenously transplanted with 3 x 10^6 cells. Right: Kaplan-
1066 Meier survival curve of mice transplanted with WT or *PPM1D*-mutant (grey) leukemia cells with
1067 or without *SOD1*-deletion. The median survival of mice transplanted with WT, WT/$SOD1^{-/-}$,
1068 $PPM1D^{mut}$, and $PPM1D^{mut}/SOD1^{-/-}$ leukemia cells was 32, 43, 32, and 55 days, respectively;
1069 Mantel-Cox test, **$p<0.01$, ***$p<0.001$.
1070

Figure 2

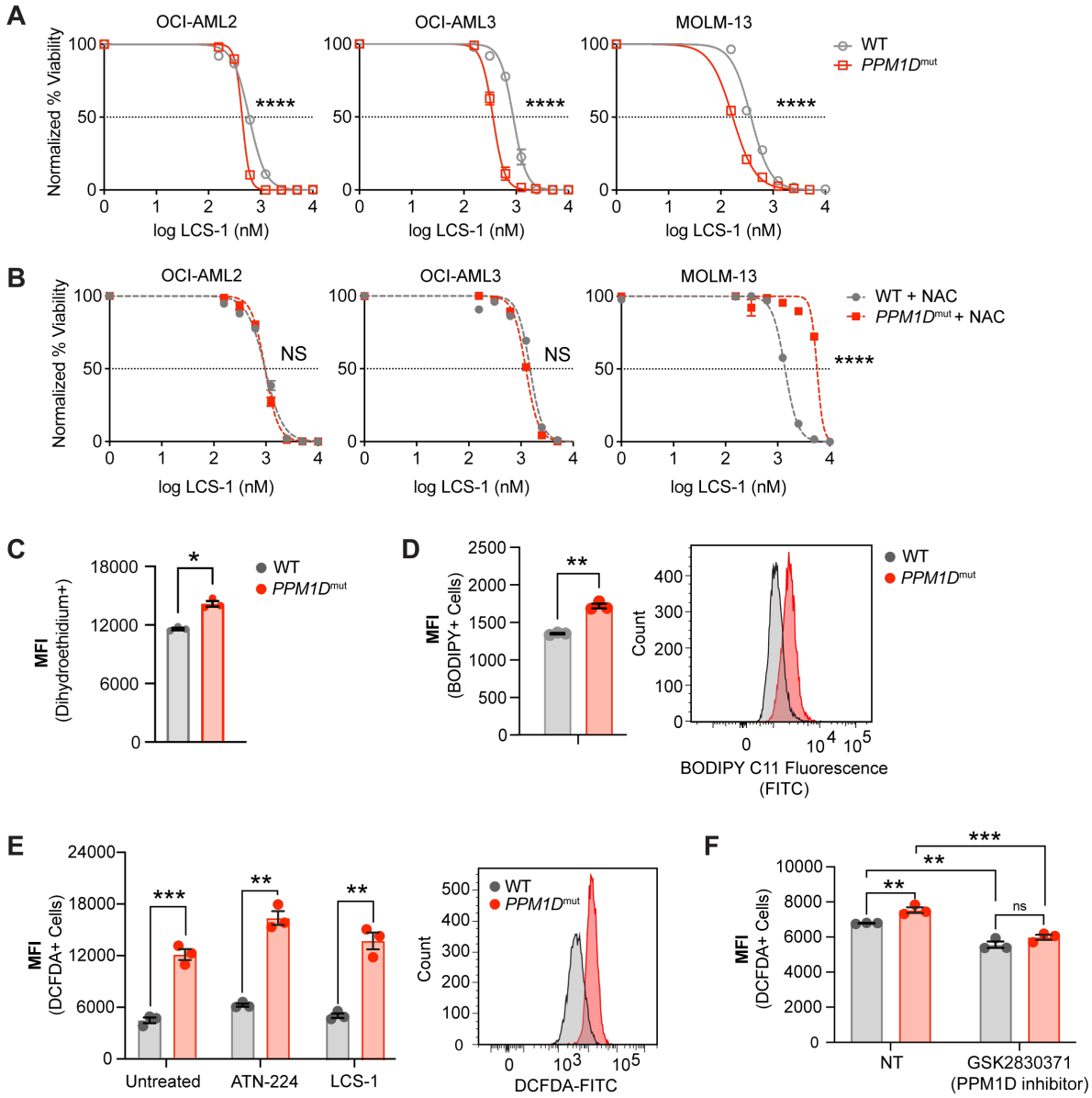
A
OCI-AML2
OCI-AML3
MOLM-13
Normalized % Viability
log LCS-1 (nM)
****
WT
PPM1Dmut
B
NS
WT + NAC
PPM1Dmut + NAC
C
MFI (Dihydroethidium+)
*
D
MFI (BODIPY+ Cells)
**
Count
BODIPY C11 Fluorescence (FITC)
E
MFI (DCFDA+ Cells)
***
**
Untreated
ATN-224
LCS-1
DCFDA-FITC
F
ns
NT
GSK2830371 (PPM1D inhibitor)

1073 **Figure 2. *PPM1D*-mutant cells are sensitive to SOD1 inhibition and have increased**
1074 **oxidative stress. (A,B)** Dose response curves for cell viability with SOD1-inhibitor (LCS-1) **(A)**
1075 or LCS-1 in combination with 0.25 uM NAC **(B)** in WT and *PPM1D*-mutant leukemia cell lines
1076 after 24-hours. Mean ± SD (n=3) is shown with a non-linear regression curve. All values are
1077 normalized to the baseline cell viability with vehicle, as measured by MTT assay. **(C)** Endogenous
1078 cytoplasmic superoxide levels of WT and *PPM1D*-mutant leukemia cell lines were measured
1079 using dihydroethidium (5 uM). The mean fluorescence intensity (MFI) of dihydroethidium was
1080 measured by flow cytometry. Mean ± SD (n=3) is shown. **(D)** Lipid peroxidation measured using
1081 BODIPY 581/591 staining (2.5 uM) of WT and *PPM1D*-mutant OCI-AML2 cells. The MFI was
1082 measured by flow cytometry. Mean ± SD (n=3) is shown. **(E-F)** Measure of total reactive oxygen
1083 species using 2',7'–dichlorofluorescin diacetate (DCFDA) staining (10 uM) measured by flow
1084 cytometry. WT and *PPM1D*-mutant OCI-AML2 cells were measured at baseline and 24-hrs after
1085 SOD1 inhibition (ATN-224 12.5 uM, LCS-1 0.625 uM) **(E)** or 24-hrs after pharmacologic PPM1D
1086 inhibition (GSK2830371, 5 uM) **(F)**; unpaired t-tests were used for statistical analyses, ns=non-
1087 significant ($p>0.05$), **$p<0.01$, ***$p<0.001$, ****$p<0.0001$.

Figure 3

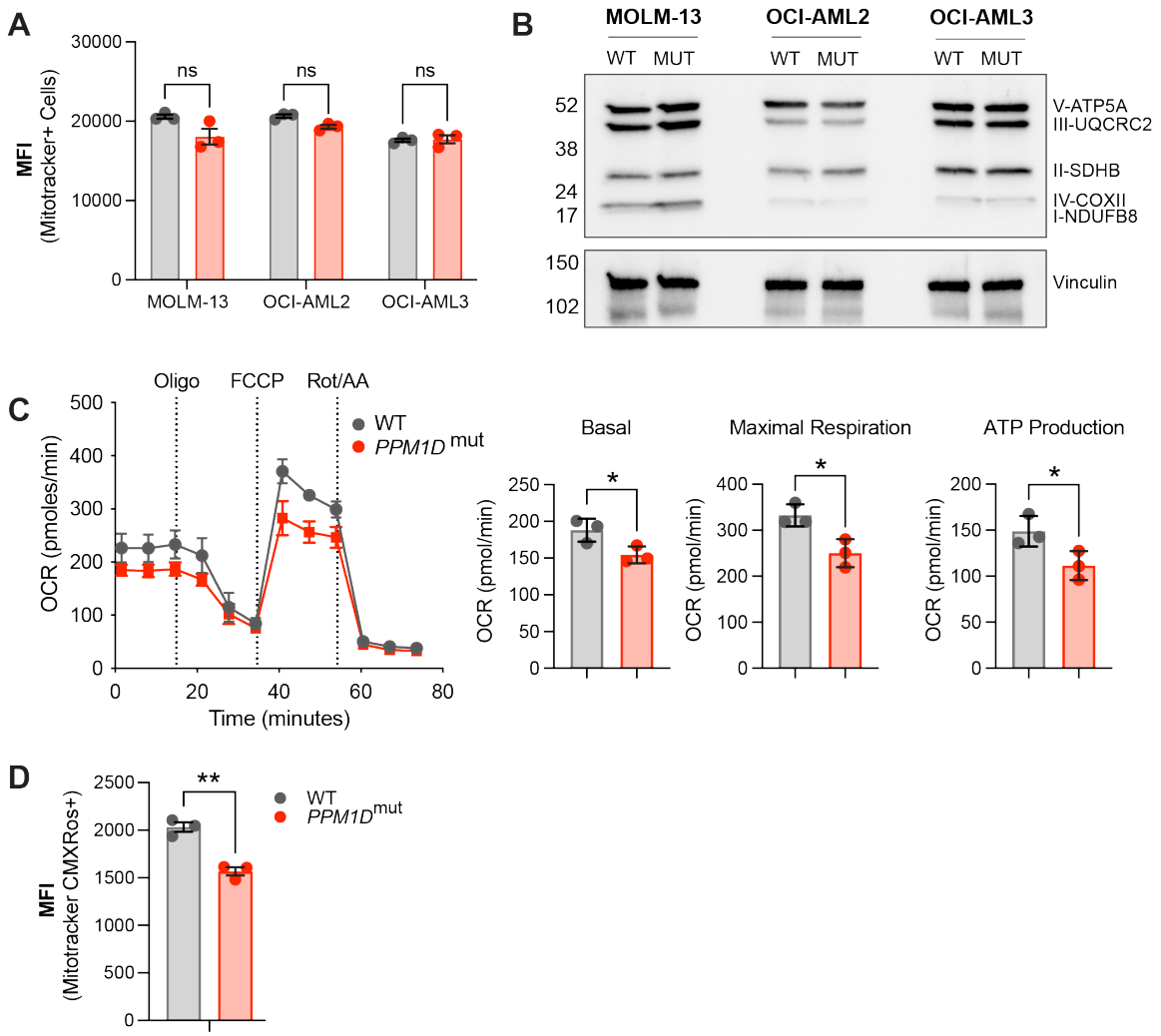

Figure 3. *PPM1D*-mutant cells have altered mitochondrial function. (A) Mitochondrial mass of WT and *PPM1D*-mutant leukemia cells was determined using MitoTracker Green (100 nM) and the mean fluorescence intensity was analyzed by flow cytometry. Data represents mean ± SD of triplicates. At least three independent experiments were conducted with similar findings; unpaired t-tests. **(B)** Immunoblot of WT and *PPM1D*-mutant cell lysates probed with the human OXPHOS antibody cocktail (1:1000) and vinculin (1:2000). **(C)** Measurement of mitochondrial oxygen consumption rate (OCR) by seahorse assay in WT and *PPM1D*-mutant OCI-AML2 cells after treatment with oligomycin (1.5 uM), FCCP (0.5 uM), and rot/AA (0.5 uM). Quantification of basal, maximal, and ATP-linked respiration are shown. Data shown are the mean ± SD of technical triplicates. **(D)** Mitochondrial membrane potential of WT and *PPM1D*-mutant OCI-AML2 cells was measured using MitoTracker CMXRos (400 nM). The mean fluorescence intensity (MFI) was measured and analyzed by flow cytometry. Data represents mean ± SD of triplicates, unpaired t-test, ns=non-significant ($p>0.05$), *$p<0.05$, **$p<0.01$.

Figure 4

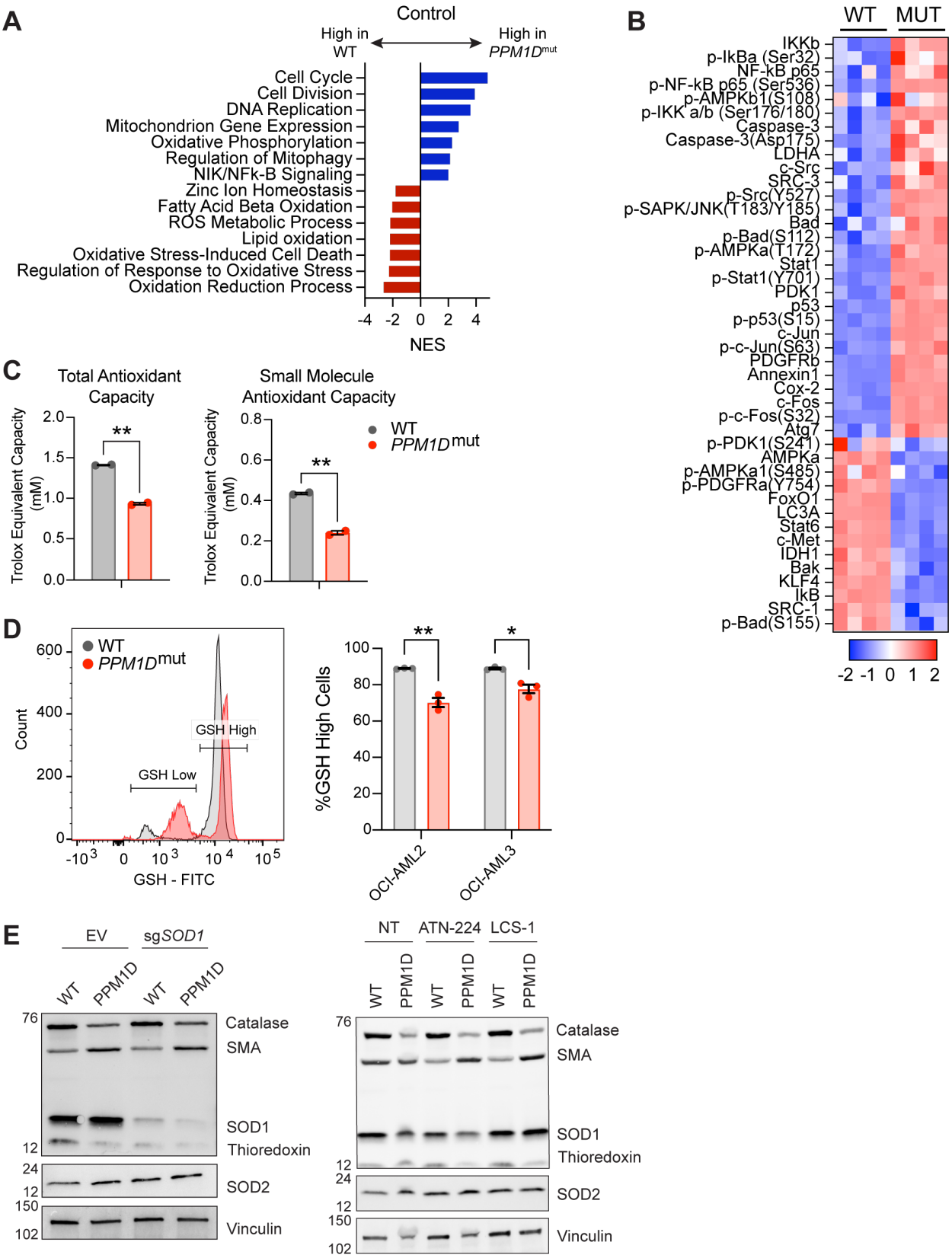

1102

1103 **Figure 4. *PPM1D*-mutant cells have a reduced oxidative stress response. (A)** RNA-seq
1104 GSEA analysis of *PPM1D*-mutant cells compared to WT Cas9-OCI-AML2 cells. Significantly up-
1105 and downregulated pathways are indicated by the blue and red bars, respectively. Normalized
1106 enrichment scores (NES) are shown with FDR <0.25. **(B)** RPPA profiling of WT and *PPM1D*-
1107 mutant OCI-AML2 cells. Proteins from the "Response to Oxidative Stress" pathway have been
1108 selected for the heatmap. Each column represents a technical replicate. See Figure 4-source data
1109 2 for the raw data. **(C)** Total- and small molecule antioxidant capacity of WT and *PPM1D*-mutant
1110 cells performed in technical duplicates. **(D)** Intracellular glutathione (GSH) levels measured by
1111 flow cytometry using the Intracellular GSH Detection kit (abcam). Left: representative flow
1112 cytometry plot demonstrating the gating for GSH-high and GSH-low populations. Right:
1113 quantification of the percentage of GSH-high cells for each cell line. Mean ± SEM (n=3) are
1114 shown. **(E)** Immunoblot of WT and *PPM1D*-mutant OCI-AML2 after transduction with the empty
1115 vector (EV) control and after *SOD1* deletion (left) or after treatment with SOD1 inhibitors for 16
1116 hours (right, ATN-224 12.5 uM, LCS-1 1.25 uM). Lysates were probed with an anti-oxidative
1117 stress defense cocktail (1:250), SOD2 (1:1000), and vinculin (1:2000). SMA=smooth muscle
1118 actin. Student t-tests were used for statistical analysis; **p<0.01, *p<0.05.
1119

Figure 5

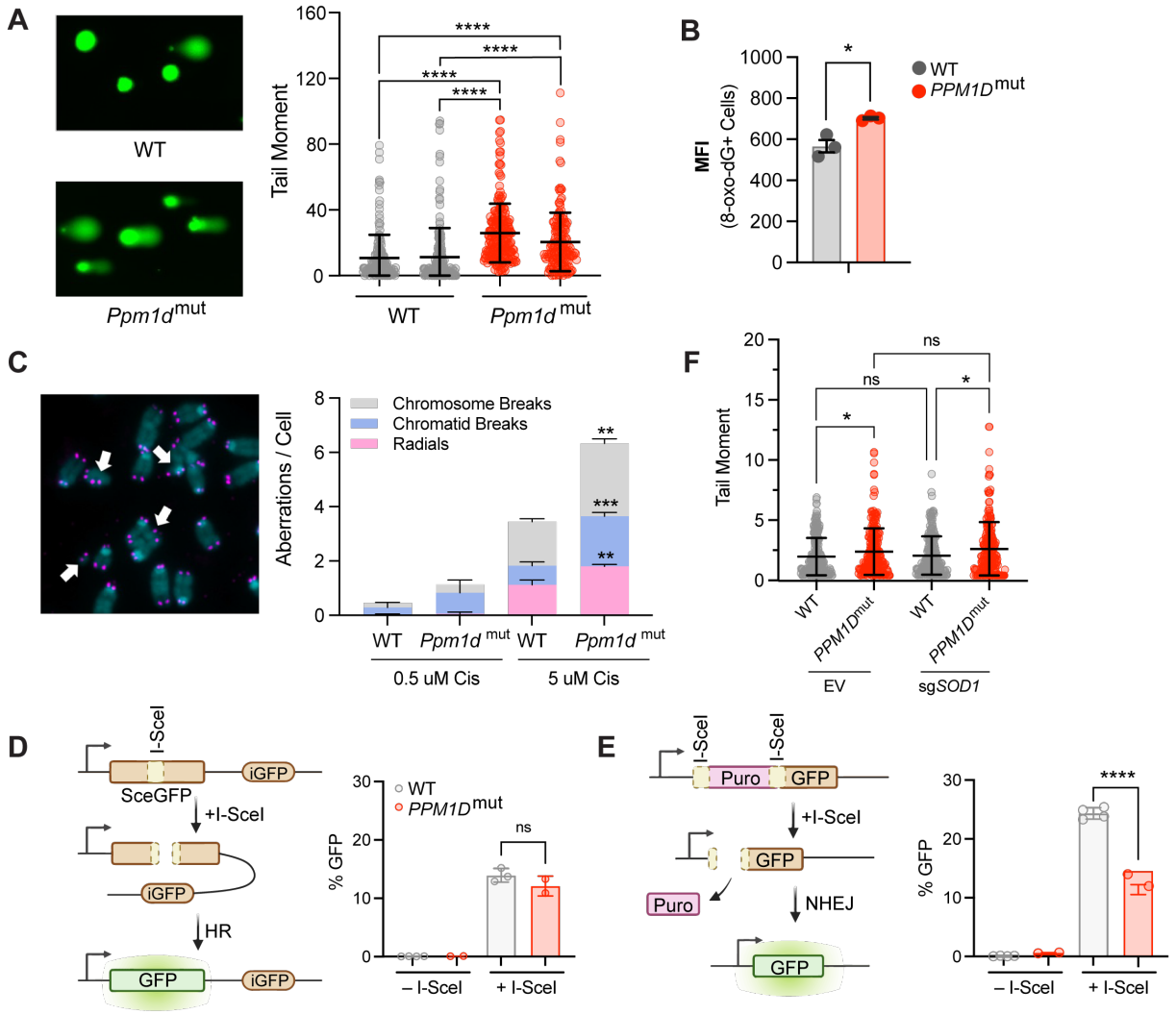
A
WT
Ppm1d mut
Tail Moment
160
120
80
40
0
****
****
****
****
WT
Ppm1d mut
B
MFI
(8-oxo-dG+ Cells)
1000
800
600
400
200
0
*
WT
PPM1D mut
C
Aberrations / Cell
8
6
4
2
0
Chromosome Breaks
Chromatid Breaks
Radials
**
***
**
WT
Ppm1d mut
WT
Ppm1d mut
0.5 uM Cis
5 uM Cis
F
Tail Moment
20
15
10
5
0
ns
ns
*
*
WT
PPM1D mut
WT
PPM1D mut
EV
sgSOD1
D
I-SceI
SceGFP
iGFP
+I-SceI
iGFP
HR
GFP
iGFP
% GFP
30
20
10
0
WT
PPM1D mut
ns
– I-SceI
+ I-SceI
E
I-SceI
I-SceI
Puro
GFP
+I-SceI
GFP
Puro
NHEJ
GFP
% GFP
30
20
10
0
****
– I-SceI
+ I-SceI

1122 **Figure 5. *PPM1D* mutations increase genomic instability and impair non-homologous end-**
1123 **joining. (A)** Left: Representative images of comet assays of mouse embryonic fibroblasts
1124 (MEFs). Two biological replicates were assessed for each genotype. Right: Quantification of
1125 n≥150 comets per experimental group with the Comet IV software; 2way ANOVA. **(B)** Mean
1126 fluorescent intensity (MFI) of 8-oxo-dG lesions within WT and *PPM1D*-mutant OCI-AML2 cells as
1127 measured by flow cytometry; student's t-test. **(C)** Left: Representative images of metaphase
1128 spreads of WT and *Ppm1d*-mutant mouse primary B-cells treated with low (0.5 uM) or high (5 uM)
1129 doses of cisplatin. Right: n≥50 metaphase cells were quantified in each experimental condition
1130 for chromosomal aberrations (white arrows). n=2 biological replicates used for each genotype.
1131 Student's t-test was used for statistical analysis. **(D–E)** Left: Schematic of the homologous
1132 recombination **(D)** or non-homologous end-joining **(E)** U2OS DNA damage repair cassettes.
1133 Right: Quantification of GFP% analyzed by flow cytometry 48-hours after induction of DNA
1134 damage by I-SceI transduction; student's t-test. **(F)** Comet assay quantification of WT and
1135 *PPM1D*-mutant Cas9-OCI-AML2 cells six days after lentiviral transduction with the empty vector
1136 (EV) control, or sg*SOD1* to induce *SOD1* deletion. Quantification and analyses of tail moments
1137 were performed using the Comet IV software. n≥150 comets were scored per experimental group;
1138 2way ANOVA. Data are mean ± SD (n=3), ns=non-significant (p>0.05), *p<0.05, **p<0.01,
1139 ***p<0.001, ****p<0.0001.

Figure 1 – Figure Supplement 1

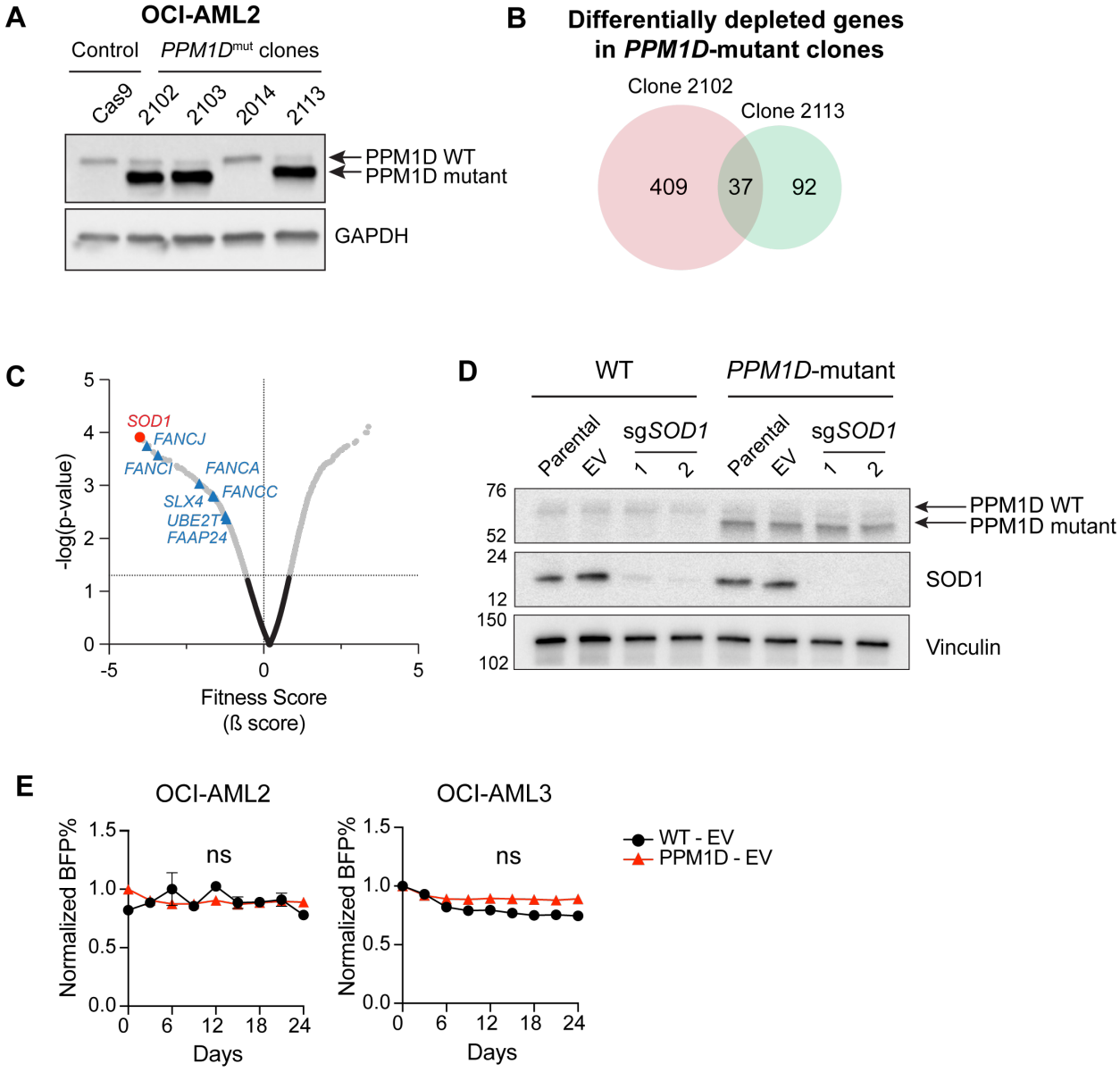

1140

1141 **Figure 1 – Figure Supplement 1. *SOD1* is a synthetic lethal vulnerability of *PPM1D*-mutant**
1142 **leukemia cells. (A)** Immunoblot validation of *PPM1D*-mutant Cas9-expressing OCI-AML2 cells
1143 generated and used for CRISPR screening. Blots were probed with anti-PPM1D (1:1000) and
1144 GAPDH (1:1000). Clones 2102 and 2113 were selected for the dropout screen. **(B)** Venn diagram
1145 of genes that were depleted from the two *PPM1D*-mutant clones (#2102, 2113) used in the
1146 dropout screen, but not depleted in the WT control lines. 37 genes were found to be depleted in
1147 both mutant clones. For a full list of genes, see Figure 1–source data 1. **(C)** Volcano plot of
1148 synthetic lethal hits ranked by fitness score with the Fanconi Anemia pathway genes highlighted
1149 in blue. **(D)** Immunoblot validation of *SOD1*-deletion. WT and *PPM1D*-mutant Cas9-OCI-AML2
1150 cells were transduced with control (EV) or sg*SOD1* lentiviruses. Two sgRNAs targeting *SOD1*
1151 were tested. Three days post-transduction, the cells underwent puromycin selection (3 ug/mL) for
1152 three days after which they were harvested for western blot. Blots were probed with anti-PPM1D
1153 (1:1000), anti-SOD1 (1:500), and anti-vinculin (1:2500). **(E)** Cas9-OCI-AML2 and Cas9-OCI-
1154 AML3 WT or *PPM1D*-mutant cells were transduced with the empty vector control backbone
1155 tagged with a blue fluorescent protein (BFP) reporter. Cells were assayed by flow cytometry
1156 between 3- and 24-days post-transduction and normalized to the BFP percentage at day 3. Data
1157 shown are mean ± SD (n=2 per condition).

Figure 2 – Figure Supplement 1

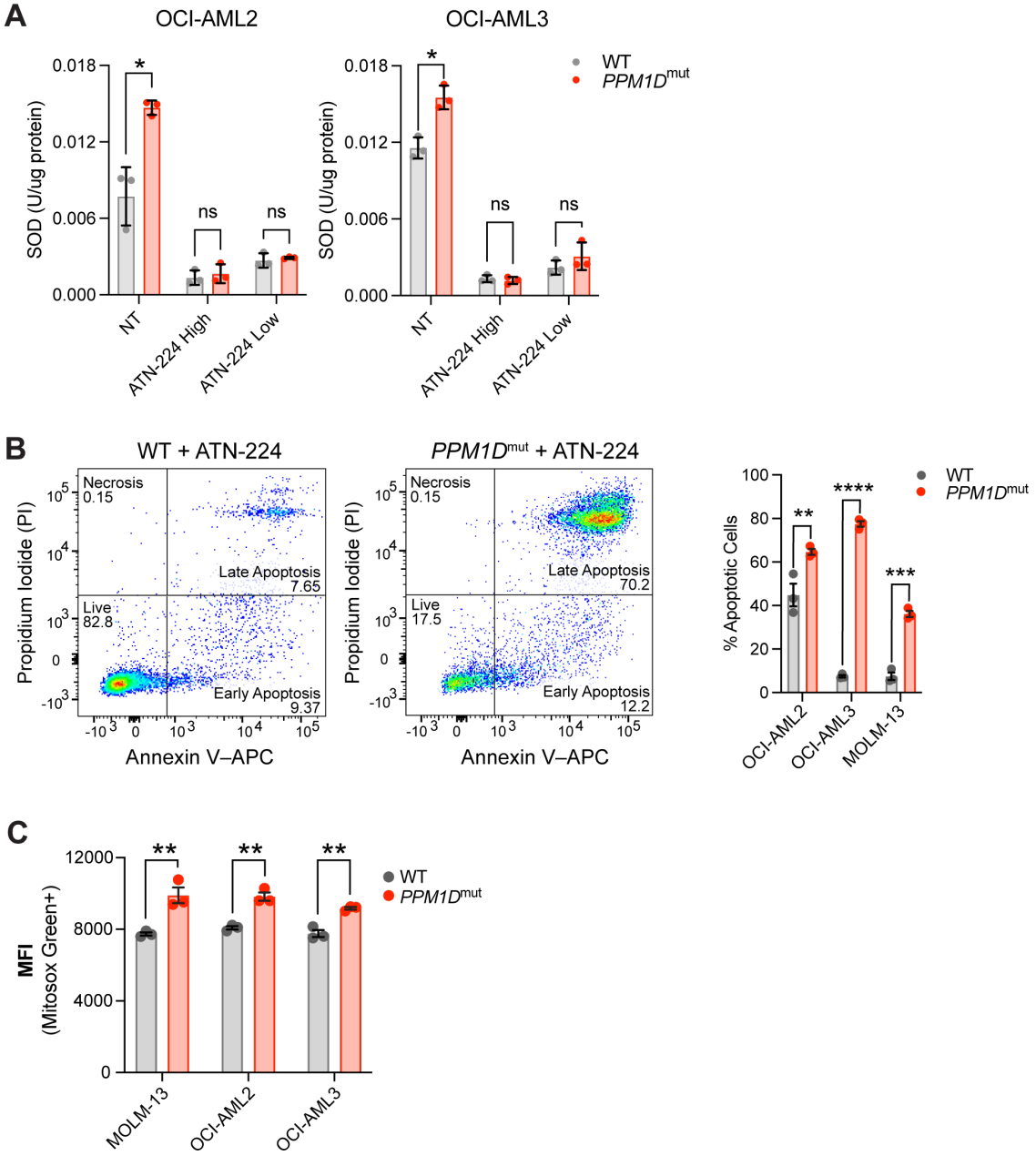

Figure 2 – Figure Supplement 1. *PPM1D*-mutant cells have increased oxidative stress. (A) SOD activity assays in OCI-AML2 and OCI-AML3 cells at baseline (NT), or treated with high (12.5 uM) or low (6.25 uM) doses of ATN-224 for 16 hours. **(B)** Left: Representative flow cytometry plots of WT and *PPM1D*-mutant cells treated with ATN-224 (25 uM for 24 hours) and stained for Annexin V-APC and PI for apoptosis; multiple unpaired t-tests, ns=non-significant, *p<0.05, **p<0.01, ***p<0.001, ****p<0.0001. **(C)** Endogenous mitochondrial superoxide levels of WT and *PPM1D*-mutant leukemia cell lines were measured using MitoSox Green staining (1 uM). The mean fluorescence intensity (MFI) of MitoSox Green was measured by flow cytometry. Mean ± SD (n=3) is shown.

Figure 2 – Figure Supplement 2

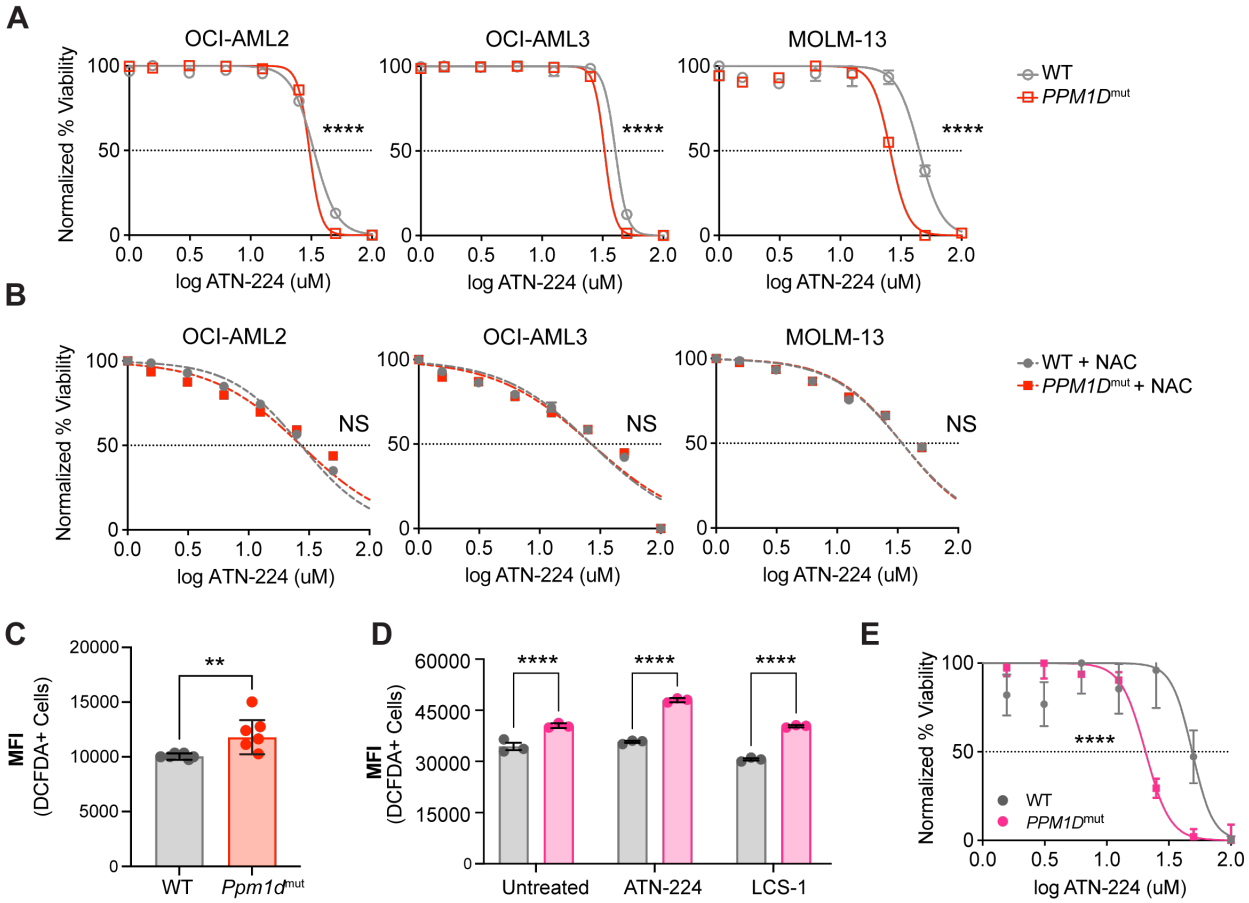

Figure 2 – Figure Supplement 2. *PPM1D*-mutant cells have increased oxidative stress. (A-B) Dose response curves for cell viability with SOD1-inhibitor (ATN-224) **(A)** or ATN-224 in combination with 0.25 uM NAC **(B)** in WT and *PPM1D*-mutant leukemia cell lines after 24-hours. Mean ± SD (n=3) is shown along with a non-linear regression curve. All values are normalized to the baseline cell viability with vehicle, as measured by MTT assay. **(C)** Total reactive oxygen species (ROS) of WT and *Ppm1d*-mutant MEFs measured by DCFDA (10 uM) staining. Mean fluorescence intensity (MFI) was determined by flow cytometry. n=6 biological replicates were used for each genotype. Data shown are the mean of each biological replicate; unpaired t-test. **(D)** Total ROS of WT GM12878 (grey) and *PPM1D*-mutant (pink) patient lymphoblastic cell lines (LCLs) at baseline, and after 24-hrs of SOD1 inhibition measured by DCFDA (10 uM) staining. MFI was determined by flow cytometry**;** multiple unpaired t-tests, **(E)** Dose response curve of WT and *PPM1D*-mutant LCLs after ATN-224 treatment. IC50s of WT and *PPM1D*-mutant LCLs were 48.8 uM and 20.51 uM, respectively as measured by MTT assay; non-linear regression analysis, ns=non-significant (p>0.05), **p<0.01, ***p<0.001, ****p<0.0001.

Figure 3 – Figure Supplement 1

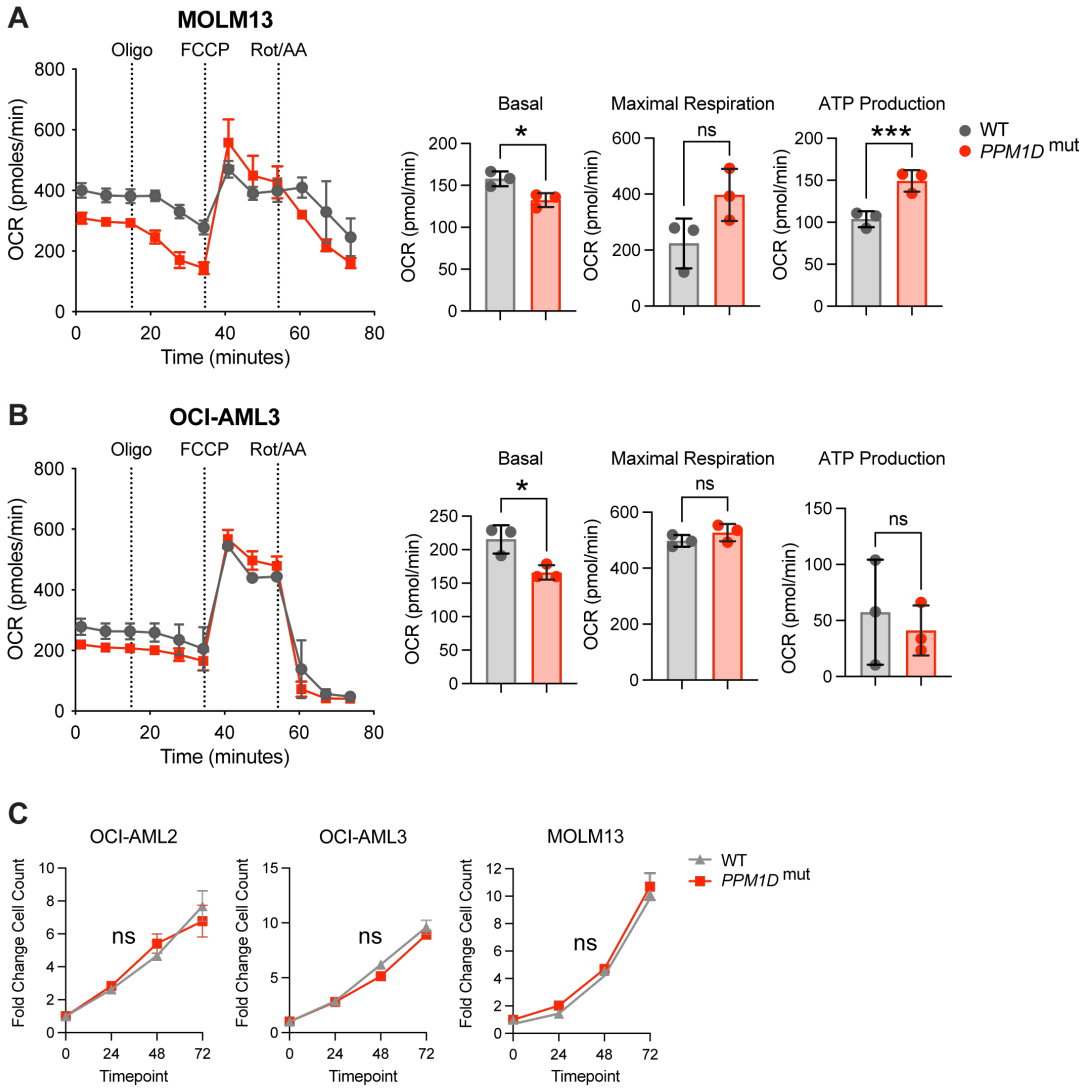

Figure 3 – Figure Supplement 1. *PPM1D*-mutant cells have altered mitochondrial function. (A,B) Measurement of mitochondrial oxygen consumption rate (OCR) by seahorse assay in WT vs. *PPM1D*-mutant MOLM-13 **(A)** and OCI-AML3 **(B)** cells after treatment with oligomycin (1.5 uM), FCCP (0.5 uM), and rot/AA (0.5 uM). Quantification of basal, maximal, and ATP-linked respiration shown. Each cell line was performed in technical triplicates, student's t-test. **(C)** Growth curves of WT and *PPM1D*-mutant leukemia cell lines at 24-, 48-, and 72-hours. Cell counts were normalized to day 0. ns=non-significant (p>0.05), *p<0.05, ***p<0.001.

Figure 4 – Figure supplement 1

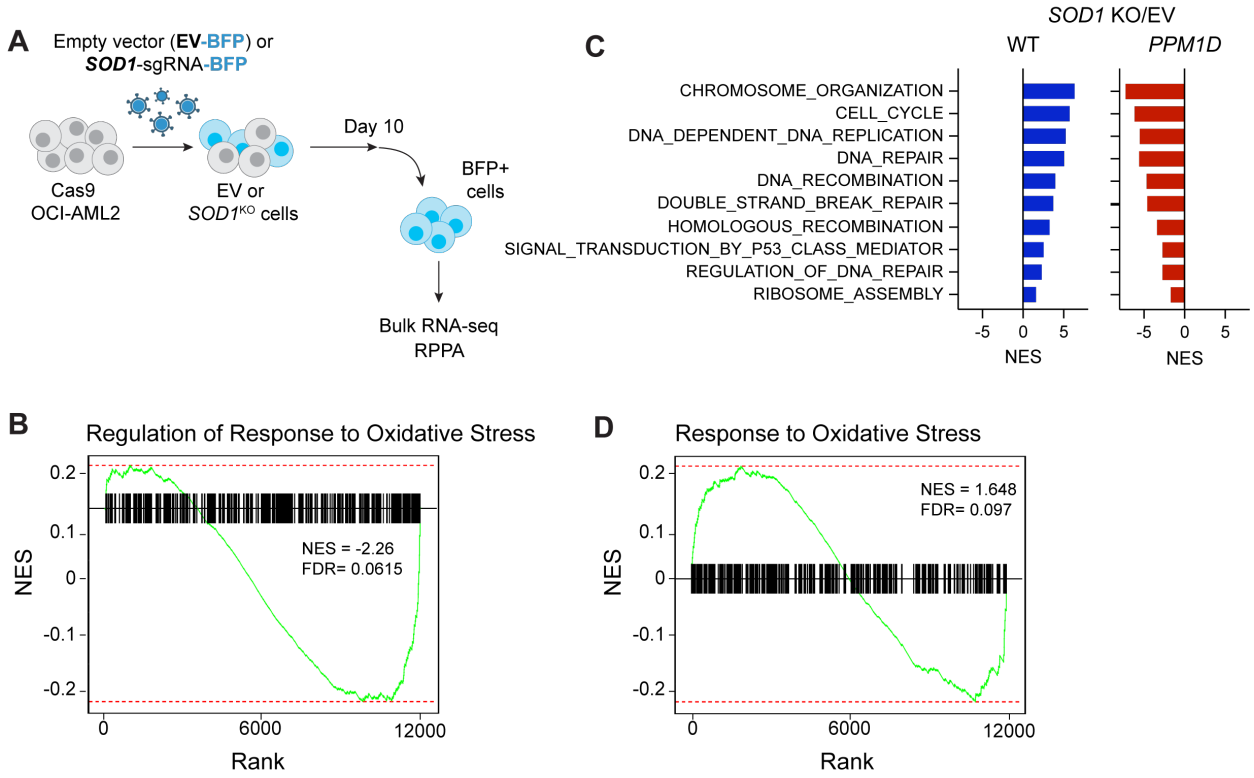

Figure 4 – Figure Supplement 1. *PPM1D*-mutant cells have reduced oxidative stress response. (A) Schematic of the experimental setup for the bulk RNA-sequencing and reverse-phase protein array. WT and *PPM1D*-mutant Cas9 OCI-AML2 cells were transduced with either empty vector (EV)-BFP or *SOD1*-sgRNA-BFP. Cells were passaged for ten days and then sorted for BFP expression for downstream analysis. **(B, D)** GSEA enrichment plots for *PPM1D*-mutant cells compared to WT after transduction with EV **(B)** or after *SOD1*-knockout **(D)** for the "Regulation of Response to Oxidative Stress" (GO:1902882) and "Response to Oxidative Stress" (GO:0006979). NES are shown with FDR<0.25. **(C)** GSEA analysis of RNA-sequencing of *SOD1*-deleted cells compared to EV control in WT and *PPM1D*-mutant cells. Blue and red bars indicate significantly up- and downregulated pathways, respectively. Normalized enrichment scores (NES) are indicated. All pathways filtered for FDR<0.25.

Figure 4 – Figure supplement 2

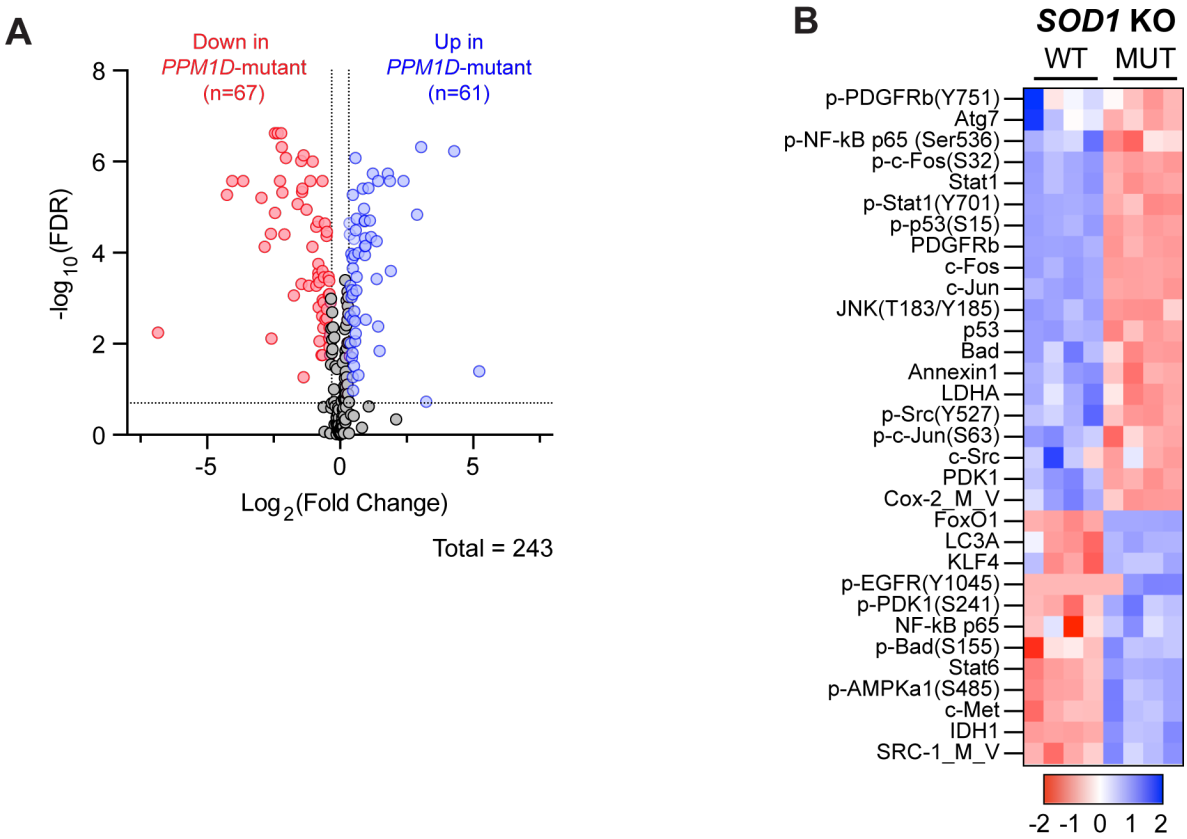

Figure 4 – Figure Supplement 2. *PPM1D*-mutant cells have reduced oxidative stress response. (A) Volcano plot of the differentially expressed proteins from the RPPA in *PPM1D*-mutant OCI-AML2 cells compared to WT. Red and blue dots indicate significantly up- or downregulated proteins, respectively, with a cutoff FDR<0.2 and linear fold change >|1.2|. **(B)** RPPA profiling of WT and *PPM1D*-mutant cells after *SOD1* deletion. Proteins from the "Response to Oxidative Stress" pathway have been selected for the heatmap. Each column represents a technical replicate. See Figure 4-source data 2 for the raw data.

Figure 5 – Figure supplement 1

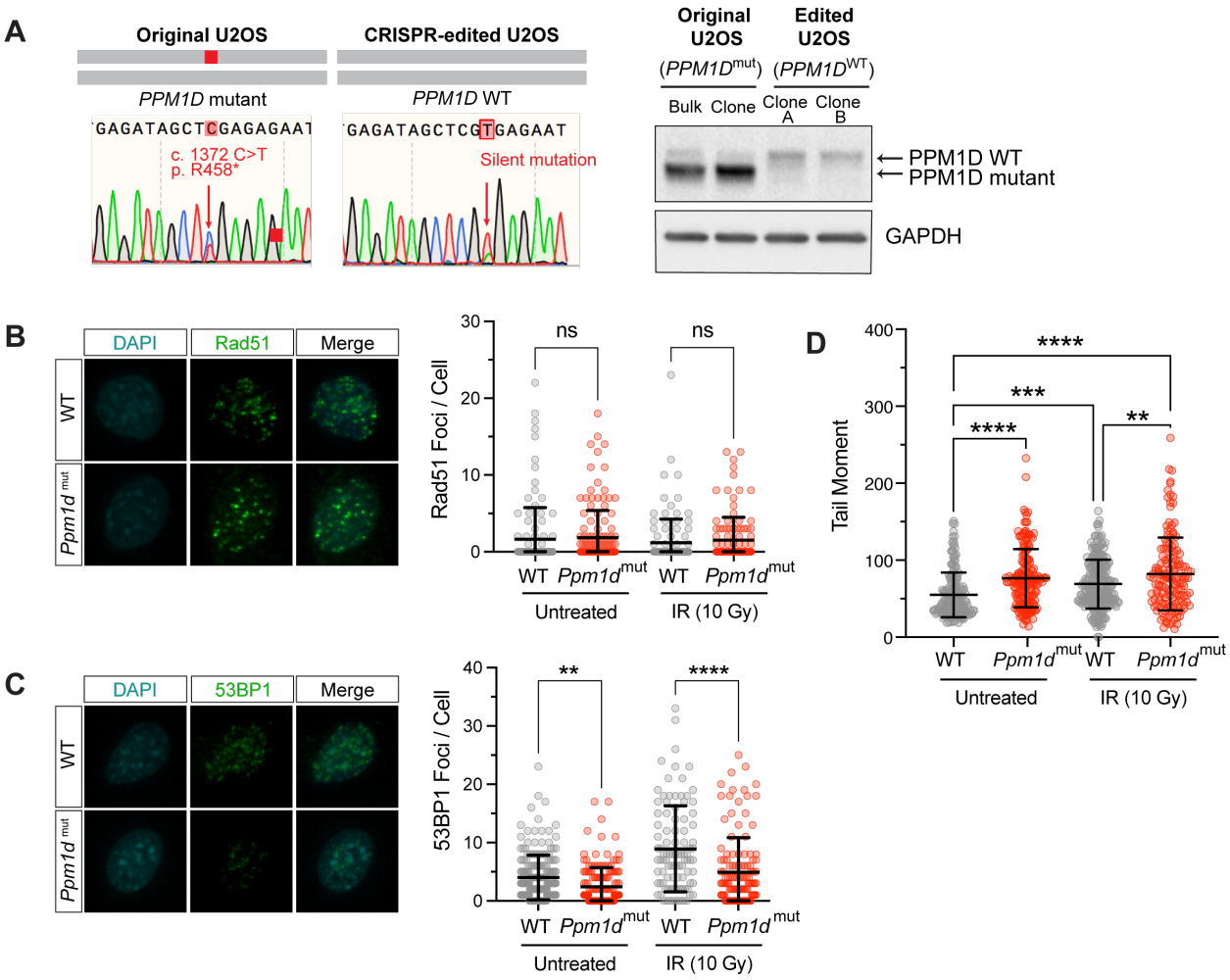

Supplementary Figure 5. *PPM1D*-mutations increase genomic instability and impairs non-homologous end-joining repair. (A) Left: Sanger sequencing traces of the parental U2OS cell line harboring a c.1372 C>T mutation in *PPM1D* and the CRISPR-edited U2OS cell line with mutation corrected to WT PPM1D. Right: Immunoblot validation of these clones are shown. Lysates were probe with anti-PPM1D (1:1000) and anti-GAPDH (1:1000). **(B,C)** Left: Representative images of Rad51 and 53BP1 immunofluorescence microscopy. Mouse embryonic fibroblasts were treated with 10 Gy irradiation, harvested 1-hour post-irradiation and stained for the indicated markers. Right: Quantification of the number of foci per cell is shown. Analysis was performed using CellProfiler. n>100 cells for each condition; students t-test. **(D)** Comet assay quantification of mouse embryonic fibroblasts at baseline and after 1-hour post-irradiation (10 Gy). Quantification and analyses of tail moments were performed using the Comet IV software. n≥150 comets were scored per experimental group; 2way ANOVA, ns=non-significant (p>0.05), *p<0.05, **p<0.01, ***p<0.001, ****p<0.0001.